

2020-07-22

A small S-MIF signal in Martian regolith pyrite: Implications for the atmosphere

Tomkins, AG

<http://hdl.handle.net/10026.1/16123>

10.1016/j.gca.2020.07.022

Geochimica et Cosmochimica Acta

Elsevier BV

All content in PEARL is protected by copyright law. Author manuscripts are made available in accordance with publisher policies. Please cite only the published version using the details provided on the item record or document. In the absence of an open licence (e.g. Creative Commons), permissions for further reuse of content should be sought from the publisher or author.

1
2
3
4
5
6
7
8
9
10
11
12
13
14
15
16
17
18
19
20
21
22
23
24
25
26
27
28
29
30

A small S-MIF signal in Martian regolith pyrite: Implications for the atmosphere

Andrew G. Tomkins¹, Sarah L. Alkemade¹, Sophie E. Nutku¹, Natasha R. Stephen², Melanie A. Finch¹, and Heejin Jeon³

1. School of Earth, Atmosphere and Environment, Monash University, Melbourne, Victoria 3800, Australia

2. Plymouth Electron Microscopy Centre, University of Plymouth, Drake Circus, Plymouth, Devon, PL4 8AA, United Kingdom

3. Centre for Microscopy, Characterisation and Analysis, University of Western Australia, 35 Stirling Highway, Perth, Western Australia 6009, Australia

*Corresponding Author Details:
Andrew Tomkins
Email: andy.tomkins@monash.edu
Phone: +61 3 9905 1643
Fax: +61 3 9905 4903

Keywords: Sulfur, sulfate, Mars, S-MIF, regolith, atmosphere

31 Abstract

32

33 The past Martian atmosphere is often compared to the Archean Earth's as both were
34 dominated by CO₂-rich and O₂-poor chemistries. Archean Earth rocks preserve mass-
35 independently fractionated sulfur isotopes (S-MIF; non-zero $\Delta^{33}\text{S}$ and $\Delta^{36}\text{S}$), originating from
36 photochemistry in an anoxic atmosphere. Thus, Martian crustal rocks might also be expected
37 to preserve a S-MIF signature, providing insights into past atmospheric chemistry. We have
38 used secondary ion mass spectrometry (SIMS) to investigate in situ, the sulfur isotope
39 systematics of NWA 8171 (paired to NWA 7034), a Martian polymict breccia containing
40 pyrite that formed through hydrothermal sulfur addition in a near-surface regolith setting. In
41 this meteorite, pyrite grains have a weighted mean of $\Delta^{33}\text{S}$ of $-0.14 \pm 0.08 \text{ ‰}$ and $\Delta^{36}\text{S} = -$
42 $0.70 \pm 0.40 \text{ ‰}$ (2 s.e.m.), so the S-MIF signature is subtle. Sulfur isotope data for four
43 additional shergottites yield $\Delta^{33}\text{S}$ values that are not resolvable from zero, as in previous
44 studies of shergottites. At first glance the result for the polymict breccia might seem
45 surprising, but no Martian meteorite yet has yielded a S-MIF signature akin to the large
46 deviations seen on Earth. We suggest that S-MIF-bearing aerosols (H₂SO₄ and S₈) were
47 produced when volcanic activity pushed a typically oxidising Martian atmosphere into a
48 reduced state. After rain-out of these aerosols, S₈ would tend to be oxidised by chlorate,
49 dampening the S-MIF signal, which might be somewhat retained in the more abundant
50 photolytic sulfate. Then in the regolith, mixing of aqueous surface-derived sulfate with
51 igneous sulfide (the latter with zero MIF), to form the abundant pyrite seen in NWA 8171,
52 would further dampen the S-MIF signal. Nonetheless, the small negative $\Delta^{33}\text{S}$ anomalies seen
53 in Martian meteorites imply that volcanic activity was sufficient to produce a reducing
54 atmosphere at times. This volcanically-driven atmospheric evolution would tend to produce
55 high levels of carbonyl sulfide (OCS). Given that OCS is a relatively long-lived strong
56 greenhouse gas, the S-MIF signal implies that volcanism periodically generated warmer
57 conditions, perhaps offering an evidence-based solution to the young wet Mars paradox.

58

59

60

61

62

1. INTRODUCTION

63 Geological evidence indicates that early in its history, during the late Noachian, the
64 Hesperian and into the early Amazonian (~4.0 – 2.8 Ga), Mars was likely warm with a
65 thicker atmosphere, rivers, lakes and glaciers, a groundwater system, and possibly a northern
66 ocean (cf. Hynek, 2016; Wordsworth, 2016; Kite, 2019; Lasue et al., 2019). Consequently,
67 many have suggested that the climate of Mars may have been suitable for life at this time
68 (e.g., Bibring et al., 2006; Michalski et al., 2017; Wordsworth, 2016), possibly analogous to
69 the early Earth (Michalski et al., 2017). However, this young wet Mars is yet to be achieved
70 by climate models (Kite, 2019), presenting a considerable paradox. Earth's atmosphere
71 evolved from initially very low O₂ concentrations (<10⁶ x Present Earth Atmospheric Level –
72 PEAL; cf. Catling & Zahnle, 2020; Pavlov and Kasting, 2002), through at least two great
73 oxidation events (e.g., Campbell and Allen, 2008; Farquhar et al., 2014), probably caused by
74 photosynthesising microorganisms (e.g., Campbell and Squire, 2010). The first great
75 oxidation event occurred at about 2.4-2.3 Ga, and is best evidenced by a distinct change in
76 the S isotope signature of sedimentary sulfide and sulfate minerals (Farquhar et al., 2014).
77 Prior to this first great oxidation event these minerals record distinct signatures of mass-
78 independently fractionated sulfur isotopes, whereas afterwards this signature disappears
79 completely (Farquhar et al., 2014).

80

81 Mass-dependently fractionated sulfur isotopes fall on mass fraction curves that closely
82 approximate straight lines, whereby $\Delta^{33}\text{S}$ and $\Delta^{36}\text{S}$ are zero ($\Delta^{33}\text{S} = \delta^{33}\text{S}_{\text{meas}} - 0.515\delta^{34}\text{S}_{\text{meas}} =$
83 0 ; and $\Delta^{36}\text{S} = \delta^{36}\text{S}_{\text{meas}} - 1.9\delta^{34}\text{S}_{\text{meas}} = 0$; Farquhar et al., 2007a). Sulfur isotope mass
84 independent fraction (S-MIF) is indicated by data that plot off these mass-dependent lines
85 ($\Delta^{33}\text{S}$ and $\Delta^{36}\text{S} \neq 0$) – these are a measure of the extent that $\delta^{33}\text{S}$ and $\delta^{36}\text{S}$ has deviated from
86 the standard mass relationship with $\delta^{34}\text{S}$. After the discovery of non-zero $\Delta^{33}\text{S}$ and $\Delta^{36}\text{S}$ in
87 Earth’s Archean sedimentary rocks (Farquhar et al., 2000a), it was determined that S-MIF
88 can be produced in reducing atmospheres via photolysis of volcanic SO_2 by ultraviolet (UV)
89 radiation (Catling and Zahnle, 2020; Endo et al., 2016; Farquhar et al., 2001). Once
90 fractionated, positive and negative $\Delta^{33}\text{S}$ exit the atmosphere in separate aerosols of opposing
91 oxidation states: S_8 with *positive* $\Delta^{33}\text{S}$ and sulfate with *negative* $\Delta^{33}\text{S}$, and the opposite
92 applies to $\Delta^{36}\text{S}$ (cf. Pavlov and Kasting, 2002; Izon et al., 2017; S_8 is a stable aerosol in
93 reducing atmospheres because it is a ring molecule). The sign of these fractionations is also
94 observed in experiments (e.g., Endo et al., 2016), although the validity of these results has
95 been questioned by Harman et al. (2018). Conceptually, if the S_8 becomes oxidised, or if the
96 sulfate is reduced, the positive and negative S-MIF reservoirs are re-homogenised, erasing
97 the S-MIF signature (Pavlov and Kasting, 2002). However, although it comes close, SO_2
98 photolysis alone cannot exactly reproduce the S-MIF trend seen in Archean Earth rocks
99 (whereby negative $\Delta^{33}\text{S}$ linearly correlates with positive $\Delta^{36}\text{S}$ and vice versa), and a range of
100 alternatives have been suggested. For example, it is possible that a mix of this mechanism
101 together with SO_2 photoexcitation is responsible (Endo et al., 2016; 2019). Recently, the
102 chain formation model (Babikov, 2017) has arisen whereby sulfur atoms derived from
103 photolysis of SO_2 are combined in low-oxygen atmospheres into progressively larger
104 allotropes ($\text{S}_2 \rightarrow \text{S}_3 \rightarrow \text{S}_4 \rightarrow \text{S}_8$), with elemental S_4 and S_8 having strongly *negative* $\Delta^{33}\text{S}$ and
105 strongly positive $\Delta^{36}\text{S}$ and the reverse in the remaining gas phases. Refinement of this model
106 by Harman et al. (2018) confirmed the negative sign of $\Delta^{33}\text{S}$ produced by the chain formation
107 model, and these authors noted that the mass-independent fractionation is much stronger than
108 in the SO_2 photolysis model. Whatever the mechanism, the MIF signature can be preserved in
109 sulfide or sulfate minerals that formed with a contribution from atmospheric sulfur (e.g.,
110 Catling and Zahnle, 2020); sulfides formed entirely from mantle-derived sulfur in magmas
111 cannot contain this signature (Labidi and Cartigny, 2016). The oxidation state of the
112 atmosphere and the depositional environment is of particular importance to S-MIF
113 preservation. Archean Earth sedimentary rocks tend to contain either sulfides with positive
114 $\Delta^{33}\text{S}$, or sulfates with negative $\Delta^{33}\text{S}$ (Farquhar et al., 2000a), although when sulfides from
115 sulfate-bearing rocks are analysed they tend to differ from sulfides in non-sulfate-bearing
116 rocks (see data in Muller et al., 2016). Given that the Martian surface is sulfate rich, this is an
117 important observation.

118
119 Analysis of the extent and variation of S-MIF on Mars throughout its history has potential to
120 provide key insights into its atmospheric evolution. Mars is thought to have maintained a
121 CO_2 -dominated atmosphere throughout its history (e.g., Catling and Kasting, 2017; Haberle
122 et al., 2017), and there is no evidence that biological processes drove extreme oxygenation of
123 the atmosphere like on Earth, and these favour preservation of S-MIF. Furthermore, Mars has
124 had active volcanoes, and abundant sulfates are preserved at multiple localities on the
125 surface, indicating vigorous aqueous sulfur mobilisation on and immediately beneath the
126 surface across a broad period of time (e.g., Gaillard et al., 2013). Thus, distinct S-MIF
127 signatures are expected to be preserved within aqueously formed or modified near-surface
128 rocks on Mars (Sholes et al., 2017).

129

130 Slightly anomalous S-MIF has been reported in seven Martian meteorites, whereas the vast
131 majority of shergottites do not have anomalous S-MIF. Very slightly positive anomalies have
132 been detected in two shergottites Northwest Africa 2990 (NWA 2990 and its pair, NWA
133 5298) and Los Angeles, and slightly negative anomalies have been reported in shergottites
134 NWA 7635 and NWA 11300, and nakhlites MIL 03346, Y000593 and Nakhla (Dottin III et
135 al., 2018; Farquhar et al., 2000b; 2007b; Franz et al., 2014; 2019; Greenwood et al., 2000).
136 These results prompted the suggestion that these igneous rocks formed from magmas that
137 may have assimilated sulfur deposited by near-surface aqueous processes (Franz et al., 2014;
138 2019). However, sulfide in Nakhla has only a subtle negative S-MIF signature ($\Delta^{33}\text{S}$ of
139 -0.09‰), whereas sulfate therein is significantly more negative ($\Delta^{33}\text{S}$ of -1.25‰ ; Farquhar
140 et al., 2007b), implying that minimal surface sulfate was assimilated by the magma. Franz et
141 al. (2014) also recognised that since the nakhlites underwent weak hydrothermal alteration
142 (Farquhar et al., 2000b; Udry and Day, 2018), they may have acquired their anomalous
143 signature after igneous emplacement. The nakhlites and chassignites all crystallised at ca.
144 1.34 Ga and are launch-paired, and so likely came from one place on Mars (Udry and Day,
145 2018), and NWA 7635 (paired with NWA 8159) likely formed at 2.37 ± 0.25 Ga (cf. Herd
146 et al., 2017). Thus, there are relatively few samples of the Martian surface with known ages and
147 anomalous S-MIF results (the age of NWA 11300 and possible pairs is unknown, though
148 likely young). All previous work has found that $\Delta^{36}\text{S}$ for Martian meteorites is unresolvable
149 from zero (Farquhar et al., 2000b; 2007b; Franz et al., 2014; 2019). Although there are
150 effectively few sample points, the observed variation in $\Delta^{33}\text{S}$ and not $\Delta^{36}\text{S}$ has been suggested
151 to indicate that Martian atmospheric chemistry was different from that of the Archean Earth
152 (Farquhar et al., 2007b). Figure 1 shows the existing $\Delta^{33}\text{S}$ data as a function of time from
153 Martian meteorites. The shergottites are here considered unlikely to have assimilated a large
154 amount of near- or at-surface sulfur (see detail in Discussion), so they are unlikely to provide
155 a sample of atmospherically modified sulfur. Therefore, because none of the previous studies
156 have been able to sample rocks that experienced extensive sulfur addition by near-surface
157 alteration, and the nakhlites and NWA 7635 only represent two points in time separated by a
158 billion years, we currently have only the vaguest idea of the past atmospheric chemistry of
159 Mars as it relates to S isotope fractionation.

160
161 In 2013, the first meteoritic sample of the Martian regolith was recovered and has since been
162 the subject of extensive research focusing on the Martian near-surface environment (Agee et
163 al., 2013; Hewins et al., 2017; see more below). NWA 7034 (and pairs: NWA 7475, 7533,
164 7906, 7907, 8114, 8171, 8674, 10922, 11220, 11522, 11896, 11921 and Rabt Sbayta 003,
165 010) is a polymict regolith breccia featuring extensive secondary alteration and abundant
166 hydrothermal sulfides from the near-surface of Mars (Humayun et al., 2013). It has been
167 suggested that high temperature lithification of the breccia occurred at around 1.35 Ga
168 (Hewins et al., 2017), although Cassata et al. (2018) found evidence for protracted heating
169 between 1.5 and 1.2 Ga. Although the ages of the hydrothermal alteration and pyrite
170 formation have not been specifically determined, the pyrite is thought to have formed at
171 $\sim 400\text{--}500^\circ\text{C}$ (cf. Lorand et al., 2018), which is hotter than the closure temperature of the
172 $^{40}\text{Ar}/^{39}\text{Ar}$ system employed by Cassata et al. (2018). Thus, one might surmise that these
173 formed through hydrothermal convection in a sub- or near-crater setting shortly after impact-
174 associated lithification, sometime, and perhaps repeatedly, within the 1.5-1.2 Ga window.
175 The Martian S-MIF record has not yet been updated to include this important sample. This
176 study examines the sulfur isotope abundances in hydrothermal pyrite in Martian regolith
177 breccia NWA 8171 by in-situ Secondary Ion Mass Spectrometry (SIMS). For comparison,
178 sulfides in several additional shergottites were also analysed by SIMS and traditional
179 petrographic techniques to investigate the hypothesis that the sulfides in some of these

180 formed in response to magmatic assimilation of surface sulfur. Our data are compared with
181 those published from other Martian meteorites and the Archean Earth S-MIF record to gain
182 insights into the atmospheric chemistry of Mars.

184 185 **2. METHODS** 186

187 Five of the shergottites examined in this study are part of the Monash University meteorite
188 collection (NWA 7320, 7397, 8656, 8716, 10170), and one, Los Angeles (BM2000, M12),
189 was previously analysed at the Natural History Museum, London, and subsequently
190 reprocessed at the University of Plymouth. We also investigated two examples of the Martian
191 polymict regolith breccia (NWA 8171 and 11220).

192
193 Reflected light microscopy was initially used to examine the petrographic and mineralogical
194 characteristics of sulfides and oxides relative to the silicate assemblage in the polymict
195 breccia and shergottites. Sulfide targets for SIMS analysis were selected based on their size
196 (>20 μm), homogeneity, and lack of fracturing.

197
198 X-Ray element maps for NWA 10170 were collected using a JEOL 7001F FEG-SEM
199 (accelerating voltage of 20 kV, 10 nA beam current, working distance of 10 mm) equipped
200 with an Oxford Instruments X-Max 50 mm² EDS detector at Plymouth Electron Microscopy
201 Centre (PEMC), within the University of Plymouth. X-Ray element maps for Los Angeles
202 were generated using a LEO 1455VP SEM at the Imaging & Analysis Centre (IAC) at the
203 Natural History Museum London (20 kV accelerating voltage, 10 nA beam current and 8 mm
204 working distance), and subsequently reprocessed at Plymouth Electron Microscopy Centre
205 using Oxford Instruments Aztec software alongside the new NWA 10170 data.

206
207 Pyrite compositions in the regolith breccia sample NWA 8171 were investigated using a
208 JEOL JXA8500 electron probe micro-analyser (EPMA) at the Commonwealth Scientific and
209 Industrial Research Organisation (CSIRO), Victoria, Australia. EMPA analyses were
210 conducted using an acceleration voltage of 20 kV, a 10 nA beam current, defocused 5 μm
211 spots, and peak counting times of 20 seconds. Analyses were calibrated using natural and
212 synthetic mineral standards measured at the beginning of the session. The EMPA was also
213 used to collect element maps of selected areas in NWA 8171 and NWA 11220. A 8.19 x 6.14
214 mm area of NWA 8171 was mapped for element abundance at 2 μm resolution operating at
215 15.0 kV acceleration voltage, beam current 100 nA and dwell time of 20 s per pixel. A 2.60 x
216 2.35 mm area covering an impact melt spherule in NWA 11220 was mapped for element
217 abundance at 1 μm resolution operating at 15.0 kV acceleration voltage, beam current 100 nA
218 and dwell time of 20 s per pixel. Synthetic standards were used for instrument calibration
219 prior to mapping. Data analysis of both scans, using cluster routines via a CSIRO-developed
220 program, CHIMAGE, was conducted to produce mineral phase maps. These mineral phase
221 maps were quantified with spot analyses on representative selections of pyroxene, feldspar,
222 sulfides and minor phases. Major and minor element analyses of pyroxene, feldspar, apatite
223 and minor phases were conducted at 15.0 kV and beam current of 20 nA with a defocused
224 beam size of 5 μm . Major and minor element analysis of pyrite was conducted at 15.0 kV
225 acceleration voltage and beam current of 100 nA with dwell times of 20 s for Fe and S, and
226 60 s for As, Co and Ni with a defocused beam size of 1 μm .

227

228

229 **2.1. Secondary Ion Mass Spectrometry analysis**

230

231 Secondary-Ion Mass Spectrometry (SIMS) was used to investigate four sulfur isotopes (^{32}S ,
232 ^{33}S , ^{34}S and ^{36}S) in individual sulfide mineral grains in NWA 8171 (polymict breccia), NWA
233 7320, NWA 7397, NWA 8656, and NWA 8716, allowing the textural relationship between
234 sulfides and the associated silicates and oxides to be retained. The analysis was performed on
235 the CAMECA IMS-1280 ion microprobe at the Centre for Microscopy, Characterisation and
236 Analysis at the University of Western Australia. Prior to analysis, samples were cleaned with
237 ethanol, and coated with 30 nm of gold to ensure conductivity across the sample surface.
238 Previously identified sulfide grains were grouped by size (>20 , >10 and >7 μm), which were
239 measured using three different primary beam conditions. A ca. 3 nA (Gaussian) Cs^+ primary
240 ion beam operating at impact energy of 20 kV was used for the >20 and >10 μm grains, with
241 20 and 10 μm raster employed, and 0.8 nA for the >7 μm grains, with 5 μm raster (creating
242 20, 10 and 7 μm craters for analysis, respectively). During analysis, removal of the gold
243 coating around the analysis spot was ensured by 45 (3nA) or 90 s (0.8nA) pre-sputter and the
244 secondary signals were auto-centered for the field aperture and entrance slit. Energy filtering
245 (30 eV window and a 5 eV offset) was used and the entrance/exit slits were set to get a mass
246 resolving power of $\sim 5,000$ $\text{m}/\Delta\text{m}$ to separate hydride interferences from the S mass peak. A
247 normal-incidence electron gun was employed to mitigate positive-charge build-up on the
248 sample potentially caused by hitting nearby silicates. All secondary S isotopes were
249 simultaneously collected (NMR regulated) using multicollection Faraday cups (^{32}S , ^{33}S and
250 ^{34}S) and an electron multiplier (^{36}S). Data were collected in several cycles with 4 s
251 integrations, where the number of analysis cycles was decided based on the secondary S
252 intensities; 20 cycles for pyrite measurements with 3nA, and 40 cycles for pyrrhotite runs
253 with 3nA and pyrite with 0.8nA primary beam. Matrix-matching reference materials, Sierra
254 pyrite and Alexo pyrrhotite (reported in [Laflamme et al., 2016](#)), were measured every third
255 analysis to correct instrumental drift and mass fractionation and determine the external
256 reproducibility for each session as described by [Laflamme et al. \(2016\)](#).

257

258 Data processing and calculations were performed following standard procedure as per
259 [Farquhar et al. \(2007a\)](#) and are reported in the conventional delta notation:

260

$$261 \delta^{34}\text{S} = 1000 \times \left(\frac{^{34}\text{S}/^{32}\text{S}}{(^{34}\text{S}/^{32}\text{S})_{\text{ref}}} - 1 \right) \quad (1)$$

262

$$263 \Delta^{33}\text{S} = 1000 \times \left[\left(\frac{^{33}\text{S}/^{32}\text{S}}{(^{33}\text{S}/^{32}\text{S})_{\text{ref}}} \right) - \left(\frac{^{34}\text{S}/^{32}\text{S}}{(^{34}\text{S}/^{32}\text{S})_{\text{ref}}} \right) 0.515 \right] \quad (2)$$

264

$$265 \Delta^{36}\text{S} = 1000 \times \left[\left(\frac{^{36}\text{S}/^{32}\text{S}}{(^{36}\text{S}/^{32}\text{S})_{\text{ref}}} \right) - \left(\frac{^{34}\text{S}/^{32}\text{S}}{(^{34}\text{S}/^{32}\text{S})_{\text{ref}}} \right) 1.9 \right] \quad (3)$$

266

267 Values are reported in per mil (‰) deviation from VCDT (Vienna Canyon Diablo Troilite),
268 as per [Ding et al. \(2001\)](#). The reported uncertainty of $\delta^x\text{S}$ (2σ or 95% confidence) for each
269 sample propagates errors associated with an internal precision, drift correction, and the
270 repeatability of the reference material. The uncertainty in $\Delta^{33}\text{S}$ is a propagation of the
271 uncertainty in $\delta^{33}\text{S}$ and $\delta^{34}\text{S}$ using equation (3) in [Laflamme et al. \(2016\)](#). Following the
272 analyses, reflected-light optical microscopy was used to assess the reliability of data by
273 checking individual analysed spots. Data from the beam craters that crossed over onto
274 silicates or oxidised fractures within the grain were discarded.

275

276

277

3. RESULTS

278

279

3.1. Sulfide Petrography of the Martian Basaltic Breccia

280
281 An extensive amount of petrography has previously been reported for the martian basaltic
282 breccia NWA 7034 and its various parings (e.g., [Gattacceca et al., 2014](#); [Goderis et al., 2016](#);
283 [Hewins et al., 2017](#); [McCubbin et al., 2016](#); [Muttik et al., 2014](#); [Santos et al., 2015](#); [Wittman](#)
284 [et al., 2015](#)), including work focusing on the sulfide formation ([Lorand et al., 2018](#); [Lorand et](#)
285 [al., 2015](#)). Thus, only additional information that pertains to the currently study is included
286 here, focusing on the sulfides.

287
288 Pyrite grains, partly oxidised on the Earth's surface, are relatively abundant in both NWA
289 8171 and NWA 11220, and we found broadly the same relationships reported by [Lorand et](#)
290 [al. \(2018\)](#) and ([Lorand et al., 2015](#)) who studied the petrography and HSE characteristics of
291 pyrite from NWA 7533. Important points are that: (1) some pyrite occurs as isolated euhedral
292 to subhedral grains in breccia matrix, clasts, and impact spherules fairly evenly disseminated
293 throughout, implying that pyrite formed late in the mineral paragenesis ([Figure 2](#)), (2) Ni-free
294 pyrite is dominant, although some pyrite grains are Ni bearing (of 39 pyrite grains analysed
295 by EMPA, six contained > 1 wt.% Ni and up to 3.2 wt.%; [Table 1](#) contains representative
296 analyses), (3) some pyrite grains occur in fine calcite veins, which cross-cut all breccia
297 lithologies. The latter pyrite grains are thought to have formed on the fracture margins in the
298 martian regolith, and later filled with calcite through hot desert weathering ([Lorand et al.,](#)
299 [2015](#)).

300
301

302 **3.2. Sulfide Petrography of the Shergottites**

303
304 The sulfide assemblage in the studied shergottites is consistently pyrrhotite dominated.
305 Individual sulfide grains contain minor pentlandite exsolution lamellae and rare chalcopyrite.
306 Sulfide abundance generally appears to be greatest in the olivine-phyric, followed by the
307 basaltic and poikilitic shergottites. Two sulfide populations can be distinguished in most
308 samples: 1) polyhedral sulfide grains between silicate crystals, and 2) shock melted sub-
309 spherical trains of sulfide grains (<10 μm) (cf. [Stoffler et al., 1991](#)). Fractured sulfides in
310 some meteorites have been partially oxidised to Fe-oxides through terrestrial weathering.

311
312 In the four shergottites analysed for sulfur isotopes by SIMS – NWA 7320, NWA 7397,
313 NWA 8656, and NWA 8716 – pyrrhotite grains are up to 150 μm in diameter; the sulfide
314 grains in NWA 10170 are too small to be analysed by SIMS. In all of the examined
315 shergottites pyrrhotite is commonly, but not exclusively, attached to Fe-Ti oxide grains
316 (compare [Figs. 3A-D](#)), and commonly associated with the late-crystallising minerals ([Figs.](#)
317 [3B and D](#)). Pyrrhotite typically contains minor pentlandite and chalcopyrite exsolution
318 lamellae ([Fig. 3C](#)).

319
320

321 **3.3. SIMS analysis of Pyrite in Regolith Breccia NWA 8171**

322
323 Twenty-two pyrite grains were analysed in situ via SIMS. After analysis, reflected light
324 microscopy was used to rule out eight data points that were compromised by overlap with
325 oxidised fractures within grains or adjacent silicate minerals. The 7 μm spots are not able to
326 sample as much material as the 10 μm spots, and tend to have higher analytical errors and be
327 more scattered (many were also ruled out due to contamination). Therefore, we focus on the
328 results yielded by the 10 μm spots. The $\Delta^{33}\text{S}$ values for these spots range from -0.22 to -0.01
329 ‰ with a weighted mean $\Delta^{33}\text{S}$ of -0.14 ± 0.08 ‰ (± 2 s.e.m.), and $\delta^{34}\text{S}$ values range from -

330 5.21 to -0.70 ‰ with a weighted mean $\delta^{34}\text{S}$ of $-2.1 \pm 1.2\text{‰}$ (± 2 s.e.m.) (Table 2, Fig. 4a).
331 Although the 2σ error bars for the individual data points (10 μm spots) overlap with the $\Delta^{33}\text{S}$
332 = 0 line in Figure 4a, the weighted mean and its error plots below the line, and we have
333 calculated 95% probability of the result being below zero. $\Delta^{36}\text{S}$ values range between -1.27 to
334 -0.13 ‰, with a weighted mean $\Delta^{36}\text{S}$ of $-0.70 \pm 0.40\text{‰}$ (± 2 s.e.m.) (Table 2, Fig. 4b). Due to
335 the lower count rate of ^{36}S compared to the other S isotopes, there is a larger associated error
336 for $\Delta^{36}\text{S}$ values. Nonetheless, we calculate a 98% probability that the result is below zero.
337 Although the data overlap the Archean Earth's S-MIF field defined by a well-known
338 complimentary relationship between $\Delta^{33}\text{S}$ and $\Delta^{36}\text{S}$ (Fig. 4d), relatively few Earth samples
339 have negative anomalism in both $\Delta^{33}\text{S}$ and $\Delta^{36}\text{S}$, and no previous study has found a
340 resolvable $\Delta^{36}\text{S}$ anomaly in a Martian meteorite. The $\Delta^{33}\text{S}$ range for NWA 8171 is compared
341 with other Martian meteorites and samples from Earth in Figure 1.

342

343 3.4. SIMS analysis of pyrrhotite in shergottites

344

345 The sulfur-isotopic compositions of shergottites NWA 7320, 7397, 8656, 8716 are provided
346 in Table 2. None of the samples analysed in this study have a resolvable mass-independent
347 signature ($\Delta^{33}\text{S} \neq 0$) at the two-sigma level. For NWA 8656, in which 12 sulfide grains were
348 analysed, $\Delta^{33}\text{S}$ values range from -0.09 to 0.06 ‰, with a weighted mean $\Delta^{33}\text{S}$ of 0.00 ± 0.05
349 ‰ (± 2 s.e.m.), $\delta^{34}\text{S}$ values range from -1.68 to -0.40 ‰ with a weighted mean $\delta^{34}\text{S}$ of -0.89
350 $\pm 0.22\text{‰}$ (± 2 s.e.m.), and $\Delta^{36}\text{S}$ values range between -0.74 to 1.45 ‰, with a weighted mean
351 $\Delta^{36}\text{S}$ of $0.32 \pm 0.34\text{‰}$ (± 2 s.e.m.). For NWA 7397, in which 8 sulfide grains were analysed,
352 $\Delta^{33}\text{S}$ values range from -0.07 to 0.11 ‰, with a weighted mean $\Delta^{33}\text{S}$ of $-0.03 \pm 0.03\text{‰}$ (± 2
353 s.e.m.), $\delta^{34}\text{S}$ values range from -0.77 to 0.59 ‰ with a weighted mean of $\delta^{34}\text{S}$ of 0.02 ± 0.28
354 ‰ (± 2 s.e.m.), and $\Delta^{36}\text{S}$ values range between -1.04 to 0.30 ‰, with a weighted mean $\Delta^{36}\text{S}$
355 of $-0.35 \pm 0.22\text{‰}$ (± 2 s.e.m.). We were only able to measure one sulfide grain in NWA
356 8716, and two in NWA 7320 (Table 2). For all meteorites the new data are consistent with
357 previous literature data for shergottites (Fig. 5). The pyrrhotite in our samples contains
358 submicron pentlandite exsolution lamellae that were unavoidably included in the SIMS spots,
359 empirically known to make no significant fractionation using 20 μm raster.

360

361

362

363

364 4. DISCUSSION

365

366 4.1. Production and preservation of S-MIF on Mars

367

368 Slightly negative $\Delta^{33}\text{S}$ values have been found by several authors in the paired Miller Range
369 nakhlite samples (MIL 090030, 090032, and 090036) and attributed to assimilation of surface
370 sulfate by lava flows (Dottin III et al., 2018; Franz et al., 2014; Mari et al., 2019). This
371 interpretation is supported by elevated oxidation state and rapid magnetite crystallisation seen
372 in these samples (Franz et al., 2014). Yamato 000593 also has sulfate and sulfide with
373 slightly negative $\Delta^{33}\text{S}$. The other nakhlites do not contain such clear evidence for assimilation
374 of surface sulfur, although there are a small number of anomalous $\Delta^{33}\text{S}$ values amongst the
375 near zero values reported for Nakhla (cf. Farquhar et al., 2007b; Franz et al., 2014; Mari et
376 al., 2019).

377

378 The slightly negative $\Delta^{33}\text{S}$ seen in the Miller Range nakhlites argue for a Martian crust
379 enriched in atmospherically modified sulfate between ~1416 and 1322 Ma (cf. Cohen et al.,
2017; Udry and Day, 2018). Intuitively, one might expect sulfides within the Martian regolith

380 breccias to at least preserve similar, if not larger, S-MIF signatures, perhaps comparable with
381 those of the Archean Earth, because the regolith has had a prolonged residence in the Martian
382 atmosphere-surface environment and a large amount of added sulfur. The abundant pyrite +
383 magnetite in NWA 7034 and pairs indicates a prolonged environment of sulfur-rich and
384 moderately reducing near-surface conditions. However, for the first time we have found that
385 the sulfur isotope ratios of hydrothermal pyrite in a Martian regolith sample (NWA 8171),
386 yield a $\Delta^{33}\text{S}$ value of only $-0.14 \pm 0.084 \text{ ‰}$ (2 s.e.m.). This value is less negative than some
387 nakhlites and only slightly distinct from the shergottites (Figs. 4, 5), and is not clearly distinct
388 from $\Delta^{33}\text{S}$ values for Earth samples younger than ~ 2.4 Ga, when the mechanisms for
389 preserving S-MIF in the geologic record are considered to have been neutralised (Fig. 1).

390
391 Production and preservation of the S-MIF bearing sulfur species is dependent on several
392 factors, as reviewed briefly in the Introduction. Our results and those of previous studies
393 suggest that one or more factors inhibited preservation of strongly mass-independently
394 fractionated sulfur on Mars, but allowed a subtle negative $\Delta^{33}\text{S}$ signature to be retained.
395 Previous studies have not detected an anomalous $\Delta^{36}\text{S}$ signature, and this has been recognised
396 as a point of difference with Earth (Franz et al., 2019), whereas we have detected a subtle
397 negative $\Delta^{36}\text{S}$ signature. Below we explore S-MIF production and survival in two stages: 1)
398 during S-MIF production in the atmosphere, and 2) after deposition of aerosols on the surface
399 when the separate S-MIF reservoirs may have different preservation potential in the regolith.

400

401 *4.1.1. S-MIF production in the Martian atmosphere*

402 Photons of UV light drive photolysis of SO_2 to $\text{SO} + \text{O}$ at < 217 nm, of SO_2 to $\text{S} + \text{O}_2$ at $<$
403 208 nm, and of SO to $\text{S} + \text{O}$ at < 231 nm wavelength (Catling and Kasting, 2017). Since O_2
404 and O_3 absorb wavelengths shorter than ~ 300 nm, S-MIF cannot occur by these mechanisms
405 in Earth's modern troposphere, although some does occur in the upper stratosphere (Whitehill
406 et al., 2015). Pavlov and Kasting (2002) determined that S-MIF will not be preserved in an
407 atmosphere with oxygen levels greater than 10^{-5} x PEAL (now considered to be 10^{-6} x PEAL;
408 Catling and Zahnle, 2020). Although experiments have achieved photolysis of SO_2 at 10^{-3} x
409 PEAL (DeWitt et al., 2010), the abundance of SO_2 used was higher than those found in
410 nature by several factors. The weak S-MIF signature in the Martian regolith could therefore
411 plausibly be explained by an atmosphere with oxygen levels sufficiently elevated to both
412 limit UV transparency (and thus photolysis of SO_2) and inhibit preservation of separate S-
413 MIF reservoirs.

414

415 Based on $^{40}\text{Ar}/^{39}\text{Ar}$ data, it has been suggested that the oxidation and sulfidation of NWA
416 7034 and pairs likely occurred over a protracted period from ~ 1500 - 1200 Ga (Cassata et al.,
417 2018). Like today, Mars at this time (and since the late Hesperian) is thought to have had a
418 thin atmosphere and thus dry climate, which allowed formation of anhydrous iron oxides like
419 hematite at the surface (Bibring et al., 2006). Presently, the partial pressure of oxygen ($p\text{O}_2$)
420 on Mars measured by the Curiosity rover is $\sim 1.4 \times 10^{-3}$ PEAL (Mahaffy et al., 2013). As this
421 value is greater than 10^{-6} PEAL, it implies that S-MIF would not currently survive in Mars'
422 atmosphere. Oxygen levels higher than 10^{-6} PEAL for the Hesperian period were recently
423 proposed by Lanza et al. (2016) after the discovery of Mn oxides by Curiosity Rover at Gale
424 Crater. Manganese oxides did not appear on Earth until after photosynthesis and a significant
425 rise of O_2 levels (cf. Planavsky et al., 2014) implying that the Hesperian atmosphere on Mars
426 was more oxidising than the present day (Lanza et al., 2016). Oxygen is primarily produced
427 in the Martian atmosphere today by UV dissociation of CO_2 and H_2O (Barth, 1974), with the
428 current observed ratio of 1:0.7 explained by dissociation of H_2O and preferential removal of
429 H from the atmosphere via escape to space (Catling and Kasting, 2017). Therefore, in the

430 wetter past (Haberle et al., 2017), there may have been more oxygen in the atmosphere than
431 today.

432
433 Confirming this notion, Sholes et al. (2017) found, in a study modelling the effects of
434 volcanic emissions on the chemistry of the Martian atmosphere from 3.5 Ga to today, that
435 oxidising conditions (with high O₂) would prevail except for periods with active volcanism,
436 when only modest volcanic emission is required to create a reducing atmosphere. These
437 authors found that with the introduction of volcanism, the atmosphere initially forms sulfate
438 aerosols under oxidising conditions, driving the system into reducing conditions through
439 oxidation of SO₂, whereupon both sulfate and S₈ aerosols could form. Whereas sulfate starts
440 to form with minimal volcanic flux, two orders of magnitude greater flux are required before
441 S₈ starts to form. Thus, early-formed sulfate would tend not to have a S-MIF signature,
442 whereas the later S-bearing aerosols would. Since the lifetime of SO₂ in the atmosphere is
443 brief (e.g., Farquhar et al., 2000b), the Martian atmosphere is likely to have switched between
444 oxidising and reducing as a function of volcanic activity. The observations of a small
445 negative Δ³³S signature in three nakhlites and the polymict breccia are consistent with some
446 weak S-MIF development leading up to the middle Amazonian (Fig. 1), and thus support the
447 work of Sholes et al. (2017).

448
449 The Sholes et al. (2017) models are, amongst other things, based on the estimated volcanic
450 emissions for Mars during the Amazonian, and the proportions of gases emitted as a function
451 of magma oxidation state and depth of emplacement, the latter derived from Gaillard et al.
452 (2013). The proportion of the different sulfur species in volcanic gases varies as a function of
453 pressure, with lower pressures favouring higher SO₂ production (Gaillard and Scaillet, 2009;
454 Gaillard et al., 2011). Therefore, the balance of volcanic H₂S and SO₂ was suggested to have
455 shifted towards greater SO₂ as the atmosphere of Mars thinned over time (Gaillard and
456 Scaillet, 2009), and this favours generation of reducing atmospheres (Sholes et al., 2017). In
457 the Sholes et al. (2019) model, volcanic emissions were input at ground level, whereas the
458 largest and probably youngest volcanoes have peaks many km above this (Olympus Mons,
459 21.2 km; Ascraeus Mons, 18.2 km; Arsia Mons, 17.8 km; Pavonis Mons 14 km; Elysium
460 Mons 13.8 km; Tharsis plateau, >5 km). This matters for two reasons. Firstly, much of the
461 emissions would have occurred at lower pressure than modelled, and this favours generation
462 of reducing atmospheres at more modest volcanic flux. Secondly, the Sholes et al. (2017)
463 models suggest that even in reducing atmospheres, O₂ would remain relatively high (10 ppm,
464 a mixing ratio two orders of magnitude lower than today's Martian atmosphere) above a
465 sharp transition at ~20 km altitude (see their Fig. 4), whereas this transition height may be
466 considerably higher given the altitude of the volcanoes. This transition height is important
467 because it affects the extent to which UV light will be blocked and S-MIF generation
468 inhibited (see more below).

469
470 Gaillard and Scaillet (2009) showed that there were extensive volcanic SO₂ emissions during
471 the construction of Tharsis (probably during the late Noachian and Hesperian; Bouley et al.,
472 2018), possibly as much as 5.4 x 10²¹ g of sulfur, with ~60% as SO₂. Before that time, the
473 higher atmospheric pressure would have limited SO₂ emissions (Gaillard and Scaillet, 2009),
474 and thus also generation of a reducing atmosphere (see Sholes et al., 2017). Although the
475 atmosphere was thicker during the Hesperian, thus requiring greater volcanic input to achieve
476 the same transition to a reducing atmosphere compared to the Amazonian (because more O₂
477 needs to be consumed by sulfate aerosolisation), the great magnitude of emission implies that
478 this was the period best suited to generation of S-MIF.

479

480 An atmospheric sulfur-bearing gas that has received relatively modest attention with regards
481 to the Archean Earth is OCS. Carbonyl sulfide is the most abundant sulfur-bearing compound
482 in Earth's modern atmosphere despite continuous SO₂ addition from volcanoes (Kryzstofiak
483 et al, 2015) because it has a significantly longer lifetime than SO₂. OCS is a strong
484 greenhouse gas and in Earth's current atmosphere is a precursor of sulfate aerosols that
485 contain stratospherically generated S-MIF (Kryzstofiak et al, 2015; Muller et al., 2016). Its
486 variation in the Amazonian atmosphere of Mars was included in the Sholes et al. (2017)
487 models. They found that with modest volcanic emissions, well within the bounds of the
488 estimated range, OCS would build to ppm levels, concomitantly with production of H₂SO₄
489 and S₈ aerosols. The stability of OCS is favoured by relatively reducing conditions and
490 elevated CO (through reactions such as 3CO + SO₂ = 2CO₂ + OCS [Oppenheimer et al.,
491 2011], and S₂ + 2CO = 2OCS, with S and S₃ able to participate in reactions equivalent to the
492 latter [Ueno et al., 2009; Sholes et al., 2017]). Martian magmas are more reduced than those
493 on Earth, and so tend to produce erupted gases (Gaillard et al., 2013) that are better suited to
494 OCS production.

495
496 It has been suggested that the S-MIF signature of Earth's Archean sulfates, can be explained
497 by contributions to the S-MIF budget by both SO₂ and OCS photolysis (Muller et al., 2016).
498 Ueno et al. (2009) found that at ppm level concentrations of OCS (3 ppm in their model,
499 although the lower limit was not determined), part of the UV spectrum is shielded such that
500 photolysis of SO₂ only occurs in the <202 nm range. Between 180 and 202 nm, SO₂
501 photolysis produces negative Δ³³S, and therefore UV shielding by OCS may explain the
502 negative signature of Archean sulfate (Ueno et al., 2009; Muller et al., 2016). However, Endo
503 et al. (2015) found that the change in Δ³³S produced by OCS shielding is smaller than in the
504 Ueno et al. (2009) model and is not required to explain the Archean Earth's isotopic record.
505 Instead experiments show that a mix of SO₂ photolysis mechanism together with SO₂
506 photoexcitation can explain Earth's record (Endo et al., 2016; 2019). Given the results of
507 Sholes et al. (2017; their figs. 3 and 4 and associated text), we suggest that the same
508 principles should apply to the Martian atmosphere, and thus the expected sign of S-MIF
509 raining out of the atmosphere as sulfate should be negative. Depending on the extent of
510 volcanism, the abundance of S₈ may be one or more orders of magnitude less than the sulfate
511 aerosol (less volcanism = larger H₂SO₄/S₈; Sholes et al., 2017). Thus, the proportion of sulfur
512 with positive Δ³³S raining out onto the surface of Mars may have been low. A caveat is that
513 the experiment-based studies of Endo et al. (2015; 2016) were generated before the chain
514 formation model of Babikov (2017), and the latter mechanism was suggested to generate
515 strongly negative Δ³³S for the S₈ aerosol. However, another potentially important observation
516 from experiments is that photolysis of OCS, which survives for much longer in the
517 atmosphere than SO₂, produces sulfur with both weakly negative Δ³³S and Δ³⁶S (Lin et al.,
518 2011), matching our results for pyrite in the Martian regolith breccia almost exactly (Fig. 4d).

519
520 OCS is that it is a strong greenhouse gas; Ueno et al. (2009) noted that OCS at 10 ppm would
521 have radiative forcing of ~60 W m⁻², about the same as that of 1% CO₂ or 100 ppm of CH₄.
522 Thus, we suggest that the young wet Mars paradox (see e.g., Kite, 2019) might be solved by
523 the temperature increase associated with volcanically induced increase in OCS. In Earth's
524 modern atmosphere ozone has similar properties (see fig. 1b of Ueno et al., 2009) and its low
525 abundance (up to 100 ppb) is sufficient to warm the stratosphere, creating an increase in
526 temperature with altitude, which inhibits vertical mixing (warm air tends not to rise into
527 warmer air). We suggest that the very large Martian volcanoes would have pushed SO₂ into
528 higher levels in the atmosphere than in the Sholes et al. (2017) models – perhaps as high as
529 50-65 km (cf. Glaze and Baloga, 2002; Wilson and Head, 2007) – where infrared absorption

530 by OCS would create a temperature inversion and a temporarily stable stratosphere, perhaps
 531 with a thermal profile similar to the modern Earth's. This would minimise blocking of SO₂
 532 photolysis by oxygen, allowing S-MIF to progress with minor blocking by OCS, which
 533 would tend to have negative Δ³³S and near zero, perhaps slightly negative Δ³⁶S. After
 534 cessation of volcanism, SO₂ would disappear from the atmosphere quickly and gradually
 535 dwindling OCS would be the sole source of S-MIF for a period, before H₂O photolysis and
 536 H₂ escape returned the atmosphere to a colder, more oxidised state. This cycle likely repeated
 537 as volcanism increased and waned over time.

538

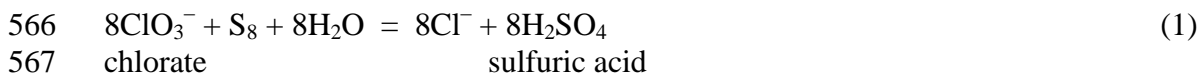
539 *4.1.2. Dampening of S-MIF signals in the regolith*

540 Preservation of S-MIF in Earth's Archean rocks is thought to have required separate delivery
 541 of the photolytic products (S₈ and H₂SO₄) from the atmosphere to the surface (Pavlov and
 542 Kasting, 2002). Conceptually, if these products are not kept isolated, their negative and
 543 positive Δ³³S values are homogenised and the S-MIF signature can be destroyed (Pavlov and
 544 Kasting, 2002). Our near-zero Δ³³S value for NWA 8171 could therefore reflect mixing, and
 545 thus cancelling out, of positive and negative S-MIF reservoirs. The vast amounts of sulfate
 546 present on the surface of Mars in sedimentary deposits and in groundwater-associated
 547 bedrock cracks (Gaillard et al., 2013; Schwenzer et al., 2016) indicate that at least the
 548 oxidised sulfur species can be delivered to the surface and preserved, but elemental sulfur has
 549 not yet been observed.

550

551 Some of the sulfate on Mars was likely produced from sulfuric acid aerosol (H₂SO₄) that
 552 rained out of the atmosphere (Gaillard et al., 2013), and this would tend to preserve negative
 553 Δ³³S, provided that some S₈ survived without oxidation in the atmosphere. Martian soils have
 554 also been found to contain relatively abundant (per)chlorate minerals (Stern et al., 2017),
 555 which are known to be strongly deliquescent at temperatures well below 273 kelvin (Gough
 556 et al., 2011; Nuding et al., 2014; Robertson and Bish, 2011; Toner and Catling, 2018); that is,
 557 they can extract H₂O from the atmosphere and then dissolve into the liquid, which can then
 558 persist down to ~200-220 K before freezing. Chlorate is known to be a strong oxidant,
 559 whereas perchlorate is kinetically inert; both are thought to be widespread in Martian soils,
 560 and chlorate is thought to have been the primary driver of the ubiquitous Fe²⁺ oxidation there
 561 (Mitra and Catalano, 2019). Perchlorate seems to be only able to oxidise nanoscale (but not
 562 microscale) Fe metal due to extremely slow reaction kinetics (Cao et al., 2005). Thus, one
 563 might expect that elemental sulfur that mixed with soils containing chlorate with attached
 564 water might be oxidised (Fig. 6) by reactions akin to:

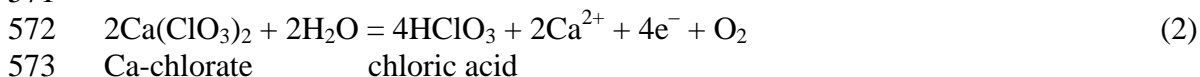
565



568

569 This redox process may also proceed in warmer, more deeply circulating waters associated
 570 with impact events (Fig. 6), perhaps via a two-step process:

571



574



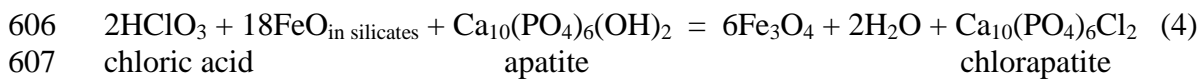
577

578 The atmospheric sulfate would have negative Δ³³S, whereas sulfate produced via Reactions
 579 1-3 would have positive Δ³³S, so mixing of these through formation of sulfate minerals in the

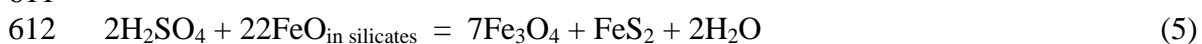
580 regolith would tend to neutralise the S-MIF signature. However, the lower proportion of S₈
 581 relative to H₂SO₄ produced in the Sholes et al. (2017) models, would allow survival of a
 582 weakened negative Δ³³S signal. The excess of chlorates in the Martian soil implies that all
 583 atmospheric sulfide would be destroyed by these reactions, provided that atmospheric
 584 humidity has periodically exceeded that required for (per)chlorate deliquescence; previous
 585 studies have found that this is the case today (Gough et al., 2011; Nuding et al., 2014). In the
 586 more distant past too, at ~1500-1200 Ma, conditions were hydrous in the deeper regolith, as
 587 indicated by the mineral assemblage of NWA 7034 and pairs (Muttik et al., 2014). The large
 588 range in δ³⁴S observed in Martian sediments implies that extensive processing of sulfur has
 589 occurred in a wet surface environment to generate strong mass-dependent fractionation
 590 (Franz et al., 2017); thus maximising the possibility of reaction between chlorates and
 591 reduced sulfur.

592
 593 Mapping by the Mars Odyssey Gamma Ray Spectrometer has revealed that chlorine is
 594 ubiquitous on the surface of Mars, particularly at low latitudes (Keller et al., 2006), implying
 595 that (per)chlorates are equivalently widespread (Carrier and Kounaves, 2015). Although we
 596 do not know the extent to which (per)chlorates pervaded the Martian regolith at ~1500-1200
 597 Ma, the relative lack of geologic activity during the Amazonian implies that the (per)chlorate
 598 distribution was comparable to today.

599
 600 NWA 7034 (and pairs) is the most oxidised Martian meteorite, containing a host of secondary
 601 minerals from hydrothermal alteration (including 15 wt % magnetite; Gattacceca et al.,
 602 2014), elevated hydration levels (Muttik et al., 2014), and elevated Cl (Williams et al., 2016).
 603 The elevated Cl in apatite suggests that some of this oxidation may have been driven by
 604 chloric acid and iron in matrix silicates, akin to:



608
 609 A magnetite-pyrite assemblage amongst hydrated minerals could also be formed through a
 610 similar reaction involving sulfuric acid, as follows:



613
 614 This reaction can explain the lack of sulfate in NWA 7034 and pairs (Hewins et al., 2017)
 615 despite the sulfate-rich surface environment of Mars, and the zero to slightly negative S-MIF
 616 signature, because sulfate carries the negative S-MIF.

617
 618 However, the pyrite in this meteorite was previously interpreted to have formed from impact-
 619 generated, near neutral and H₂S and/or HS⁻ bearing hydrothermal fluids after magnetite
 620 formation (Lorand et al., 2015; no mechanism for generation of the reduced sulfur species
 621 was suggested). Pyrite formation involving photolytically derived reduced sulfur in fluids
 622 could occur via reactions like:



625
 626 Continued fluid interaction could then remove the FeS via:



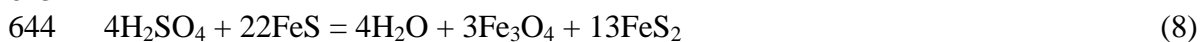
629

630 In general, [Reactions 6 and 7](#) could be pathways to preserve a positive $\Delta^{33}\text{S}$ signal of
631 photolytically produced atmospheric sulfide in the Martian regolith. Although regolith pyrite
632 produced by this mechanism may be present in some places on Mars, the slightly negative
633 $\Delta^{33}\text{S}$ of the pyrite in NWA 7034 and pairs suggests that it cannot explain the pyrite there, and
634 thus [Reactions 4 and 5](#) are the preferred mechanisms.

635

636 The [Lorand et al. \(2015\)](#) suggestion that a near neutral H_2S -bearing fluid was involved, was
637 based on the assumption that magmatic sulfide was not present in the breccia at the time of
638 hydrothermal alteration. However, if pyrrhotite was present, and it is typically present in
639 Martian mafic crust (our observation of 26 Martian meteorites), this would allow
640 equilibration with groundwater sulfuric acid, which in turn would dampen the negative S-
641 MIF of the sulfate towards zero (Martian magmatic sulfide has $\Delta^{33}\text{S} = 0.0015 \pm 0.0016\%$;
642 [Franz et al., 2019](#)), consistent with the observed results:

643



645

646 The high ratio of the zero to negative S-MIF in this reaction (22:4) implies that the
647 dampening effect would be strong. This mechanism is also consistent with the most probable
648 origin of S in the fluids; i.e., dissolution of the ubiquitous sulfates in the circulating
649 groundwater, for which [Schwenzer et al. \(2016\)](#) provided clear evidence. The high Ni
650 contents of some pyrite grains is also consistent with sulfidation of pentlandite-bearing
651 pyrrhotite, which is common in shergottites. This sort of scenario is similar in some ways to
652 the dampened S-MIF signal seen in hydrothermal volcanogenic sulfide systems in Archean
653 Earth rocks, in which modest proportions of atmospheric S contribute to the overall budget
654 ([Jamieson et al., 2013](#); [Chen et al., 2015](#)). A schematic representation of the position of NWA
655 7034 and pairs in the context of the above discussion is shown in [Figure 6](#).

656

657

658 **4.2. On magmatic assimilation as a mechanism to achieve non-zero $\Delta^{33}\text{S}$ in shergottites**

659

660 Only a fraction of shergottites would be capable of having a S-MIF anomaly because this can
661 only be achieved through contamination with sulfur affected by photolysis in the atmosphere,
662 which occurs when erupting lavas thermally erode their substrates. On Earth, this surface
663 contamination and resulting S-MIF anomaly is seen in Archean komatiite-hosted Ni sulfide
664 mineral deposits ([Bekker et al., 2009](#)). In these, field relationships clearly show that the
665 extremely hot ($>1600^\circ\text{C}$; [Sossi and O'Neill, 2016](#)) low viscosity, ultramafic lavas eroded
666 through sulfidic surface materials, causing early sulfide saturation and segregation of the
667 liquid sulfides to form ore deposits enriched in Ni, Cu and PGE ([Groves et al., 1986](#)).
668 Basaltic shergottite lavas are not as hot and are more viscous than komatiite lavas, and would
669 have been typically flowing over largely basaltic surfaces, so they would have lessened
670 ability to thermally erode their substrates. Nonetheless, calculations indicate that thermal
671 erosion is possible on Mars, and lava channels have been observed ([Williams et al., 2005](#)),
672 indicating that mild erosion has occurred in some places. Indeed, most shergottites have $\Delta^{33}\text{S}$
673 within error of zero ([Franz et al., 2014; 2019](#)), including those examined here ([Table 2, Fig.](#)
674 [5](#)).

675

676 The four shergottites identified so far with subtly anomalous S-MIF (NWA 2990, Los
677 Angeles, NWA 11300, and NWA 7635) were suggested to have attained their $\Delta^{33}\text{S}$ signatures
678 by this mechanism ([Franz et al., 2014; 2019](#)). However, with the exception of NWA 7635,
679 several factors suggest that sulfide saturation occurred late in the crystallisation history of

680 these basalts, implying that S addition did not occur. Firstly, the non-depleted concentrations
681 of Ni and Co in the bulk rock in NWA 2990 and Los Angeles (no data for NWA 11300), and
682 in olivine in NWA 2990 (Yang et al., 2015), indicate late sulfide saturation because these
683 metals are chalcophile and thus become depleted from the magma upon sulfide saturation.
684 Consistent with this, the sulfides in NWA 10170 (paired to 2990) and Los Angeles are
685 commonly in association with iron-titanium oxides (Fig. 3), suggesting that considerable
686 crystallisation occurred before sulfur saturation, which was probably achieved by loss of FeO
687 from the silicate liquid upon oxide crystallisation (cf. O'Neill & Mavrogenes, 2002). In
688 addition, the O isotopes for NWA 2990 and Los Angeles are not offset from the typical
689 Martian value (Ali et al., 2016; Bunch et al., 2009), which might be expected in a surface
690 contamination scenario, given the anomalous O isotope data of regolith breccia NWA 7034
691 and pairs (cf. Wittman et al., 2015). Because the Martian surface has been accumulating
692 meteorite and micrometeorite debris for billions of years (Tomkins et al., 2019), another
693 indicator of surface contamination might be unusually elevated HSE abundances. The
694 regolith breccia meteorites are HSE enriched (Goderis et al., 2016), and the surface-
695 contaminated Miller Range nakhlite samples are subtly HSE enriched (Mari et al., 2019),
696 whereas neither Los Angeles nor NWA 2990 (and pairs) are HSE enriched (Yang et al.,
697 2015), again suggesting minimal surface contamination. The oxidation state of Los Angeles
698 is also not elevated (McSween Jr. and McLennan, 2014), which would be expected if it had
699 assimilated sulfate.

700

701 Together, the various points above suggest that NWA 2990 and Los Angeles were not
702 contaminated by surface material, and the validity of the slightly positive $\Delta^{33}\text{S}$ result is
703 perhaps questionable (there are insufficient data for NWA 11300 currently). However, NWA
704 7635 contains considerably more sulfur than other shergottites, and launch-paired NWA 8159
705 contains no sulfides (Herd et al., 2017) and no Ni in olivine (Shearer et al., 2019), suggesting
706 that the former might be sulfide enriched and the latter sulfide depleted, and this would be
707 consistent with the slightly negative $\Delta^{33}\text{S}$ for NWA 7635 (Franz et al., 2019). NWA 7635 and
708 NWA 8159 are also magnetite-rich and oxidised (cf. Lapen et al., 2017; Herd et al., 2017;
709 Shearer et al., 2019), consistent with sulfate assimilation (see more in Shearer et al., 2019).

710

711

712 **4.3. Insights into comparative atmospheric evolution on Mars and Earth**

713

714 The earliest part of Earth's history accessed by rocks, from 3.9 to 2.4 Ga, has a continuous
715 record of non-zero $\Delta^{33}\text{S}$, and this signature is thought to have been removed by a dramatic
716 rise in atmospheric oxygen driven by photosynthesising microorganisms. One might
717 therefore ask why there appears to be more oxygen on Mars, inhibiting a strong S-MIF
718 signature, when there is no detectable sign of photosynthesising life? We know that oxygen is
719 produced in the Martian atmosphere by photodissociation of H_2O and then loss of H to space,
720 and this is likely to have been true in the wetter past, but this is the case for the early Earth
721 too. The answer appears to lie not in asking why there is oxygen in the Martian atmosphere,
722 but why there was so little in the Archean Earth's.

723

724 On Earth, the deep and extensive oceans were ferruginous during the Archean, with huge
725 quantities of dissolved Fe^{2+} (Bekker et al., 2010). This reduced iron buffered the atmospheric
726 composition by removing oxygen as iron oxide precipitate, which at times formed
727 widespread banded iron formations. Biological methane formation would have a similar
728 effect, and has been suggested as an explanation for the increase in S-MIF signal seen
729 between 2.7 and 2.4 Ga (Zahnle et al., 2006). Photosynthesising life is thought to have arisen

730 at ~2.7 Ga, but the large rise in atmospheric oxygen only occurred at ~2.4 Ga after reduced
731 iron had largely been removed from the upper oceans (Bekker et al., 2010), and methane
732 from the atmosphere (Zahnle et al., 2006). On Mars, the only significant iron oxide
733 accumulation is found in the spatially limited Meridiani Planum, and here it was only
734 precipitated in association with small bodies of standing water (Christensen and Ruff, 2004;
735 Squires et al., 2004). There is also no evidence of extensive biological methanogenesis. These
736 observations indicate that Mars as a planet had a limited capacity to buffer atmospheric
737 oxygen to very low levels, allowing build-up of sulfate minerals (since the late Noachian;
738 Bibring et al., 2006), (per)chlorates and nitrates, and minimising the opportunity for
739 development of a strong S-MIF signature.

740
741

742 5. CONCLUSIONS

743

744 Through SIMS analysis of pyrite in polymict breccia NWA 8171 we have presented new
745 multiple sulfur isotope data for the Martian regolith, supplemented with new data for four
746 additional shergottites. The polymict breccia is the most intensely sulfidised sample of all
747 Martian meteorites, and yet has only a subtle S-MIF signature; $\Delta^{33}\text{S}$ of $-0.14 \pm 0.08 \text{ ‰}$ and
748 $\Delta^{36}\text{S} = -0.70 \pm 0.40 \text{ ‰}$ (2 s.e.m.). Given this result, and considering all sulfur isotope data for
749 Martian meteorites, it appears that the Martian atmosphere is not a good analogue of Earth's
750 atmosphere during the Archean eon when life is likely to have arisen. During this period on
751 Earth there was extensive mass-independent fractionation of sulfur in an extremely oxygen
752 deficient atmosphere, which is recorded as a strongly positive $\Delta^{33}\text{S}$ signature in sedimentary
753 sulfides and negative $\Delta^{33}\text{S}$ signal in sulfates. By comparison Martian meteorites have, at
754 most, a subtly negative $\Delta^{33}\text{S}$ signature and zero to slightly negative $\Delta^{36}\text{S}$, despite having had
755 a CO_2 -dominated atmosphere for billions of years.

756

757 Having explored a range of possibilities to explain the S-MIF signature on Mars, we suggest
758 that the sulfur isotope results reflect a combination of processes. Firstly, Mars has had a long
759 history of having water ice, and sometimes liquid water, sparsely present at the surface,
760 including today. So, for over four billion years there has been photolysis of H_2O into H_2 and
761 O_2 in the atmosphere, and only modest concentrations of O_2 are needed to inhibit SO_2
762 photolysis to produce S-MIF. Nonetheless, previous modelling (Sholes et al., 2017) suggests
763 that relatively modest volcanism would release a gas mix sufficient to create globally
764 reducing conditions for brief periods. The resulting atmospheric evolution produces high
765 levels of H_2SO_4 aerosol and a lesser amount of S_8 aerosol, which would rain out, and elevated
766 OCS gas, which persists in the atmosphere. Within the regolith environment, chlorate would
767 act to oxidise S_8 , dampening the S-MIF signal. The magnetite and pyrite seen in the polymict
768 breccia meteorites were likely a product of oxidation of silicates by chlorate and sulfidation
769 of magnetite and magmatic sulfides (which have zero S-MIF) by sulfuric acid, with this
770 mixing further dampening, but not completely removing, the S-MIF carried in the sulfate.

771

772 On the Archean Earth extensive biological methane production and enormous amounts of
773 reduced iron in the oceans ensured persistence of a low oxygen atmosphere, whereas neither
774 of these were present on Mars. The amount of volcanism outgassing SO_2 has also historically
775 been smaller on Mars than Earth, thus leading to weaker S-MIF production. However, the
776 construction of Tharsis is thought to have released large amounts of SO_2 into the atmosphere,
777 eventually producing the extensive sulfate deposits on the Martian surface. The observed
778 small negative $\Delta^{33}\text{S}$ anomalies imply that volcanic activity was sufficient to produce a
779 reducing atmosphere at times, with elevated levels of OCS . Given that OCS is a strong,

780 relatively long-lived greenhouse gas, the S-MIF signal implies that volcanism periodically
781 generated warmer conditions, perhaps solving the young wet Mars paradox.

782

783

784

785

6. ACKNOWLEDGEMENTS

786

787 Nick Wilson and Colin MacRae are thanked for their assistance with the electron microprobe
788 work. We thank Junnel Alegado for preparing polished mounts of the analysed samples. We
789 acknowledge the Australian Microscopy & Microanalysis Research Facility, AuScope, the
790 Science and Industry Endowment Fund, and the State Government of Western Australian for
791 contributing to the Ion Probe Facility at the Centre for Microscopy, Characterisation and
792 Analysis at the University of Western Australia. Two anonymous reviewers and the
793 Associate Editor are thanked for their constructive comments, which have helped to produce
794 an improved paper.

795

796

797

7. AUTHOR CONTRIBUTIONS

798

799 The project was conceptualized by A.G.T., and S.L.A. and S.E.N. completed 4th year
800 research projects on NWA 8171 (S.L.A.) and the sulfide systematics of shergottites (S.E.N.)
801 under his supervision. A.G.T. adapted their work to compile the paper. N.S. assisted with the
802 petrography and edited the manuscript. M.A.F. advised on the statistics associated with the S
803 isotope data. H.J. provided technical support for the SIMS work and processed the S isotope
804 data.

805

806

8. REFERENCES

- 807
808
809 Agee, C.B., Wilson, N.V., McCubbin, F.M., Ziegler, K., Polyak, V.J., Sharp, Z.D.,
810 Asmerom, Y., Nunn, M.H., Shaheen, R., Thiemens, M.H., Steele, A., Fogel, M.L.,
811 Bowden, R., Glamoclija, M., Zhang, Z. and Elardo, S.M. (2013) Unique meteorite from
812 early Amazonian Mars: water-rich basaltic breccia Northwest Africa 7034. *Science* **339**,
813 780-785.
- 814 Ali, A., Jabeen, I., Gregory, D., Verish, R. and Banerjee, N.R. (2016) New triple oxygen
815 isotope data of bulk and separated fractions from SNC meteorites: Evidence for mantle
816 homogeneity of Mars. *Meteorit. Planet. Sci.* **51**, 981-995.
- 817 Babikov, D. (2017) Recombination reactions as a possible mechanism of mass-independent
818 fractionation of sulfur isotopes in the Archean atmosphere of Earth. *Proc. Nat. Acad. Sci.*
819 **114**, 12.
- 820 Barth, C.A. (1974) The atmosphere of Mars. *Ann. Rev. Earth Planet. Sci.* **2**, 333-367.
- 821 Bekker, A., Barley, M.E., Fiorentini, M.L., Rouxel, O.J., Rumble, D. and Beresford, S.W.
822 (2009) Atmospheric sulfur in Archean komatiite-hosted nickel deposits. *Science* **326**,
823 1086-1089.
- 824 Bekker, A., Slack, J.F., Planavsky, N., Krapez, B., Hofmann, A., Konhauser, K.O. and
825 Rouxel, O.J. (2010) Iron formation: The sedimentary product of a complex interplay
826 among mantle, tectonic, and biospheric processes. *Econ. Geol.* **105**, 467-508.
- 827 Bibring, J.-P., Langevin, Y., Mustard, J.F., Poulet, F., Arvidson, R., Gendrin, A., Gondet, B.,
828 Mangold, N., Pinet, P., Forget, F. and team, t.O. (2006) Global mineralogical and aqueous
829 Mars history derived from OMEGA/Mars Express data. *Science* **312**, 400-404.
- 830 Bouley, S., Baratoux, D., Paulien, N., Missenard, Y. and Saint-Bézar, B. (2018) The revised
831 tectonic history of Tharsis. *Earth Planet. Sci. Lett.* **488**, 126-133.
- 832 Bunch, T.E., Irving, A.J., Wittke, J.H., Rumble III, D., Korotev, R.L., Gellissen, M. and
833 Palme, H. (2009) Petrology and composition of Northwest Africa 2990: A new type of
834 fine-grained, enriched, olivine-phyric shergottite, 40th Lunar and Planetary Science
835 Conference, p. 2272.
- 836 Campbell, I.H. and Allen, C.M. (2008) Formation of supercontinents linked to increases in
837 atmospheric oxygen. *Nature Geosci.* **1**, 554-558.
- 838 Campbell, I.H. and Squire, R.J. (2010) The mountains that triggered the late Neoproterozoic
839 increase in oxygen: The second Great Oxidation Event. *Geochim. Cosmochim. Acta* **74**,
840 4187-4206.
- 841 Cao, J.S., Elliott, D. and Zhang, W.X. (2005) Perchlorate reduction by nanoscale iron
842 particles. *J. Nanoparticle Res.* **7**, 499-506.
- 843 Carrier, B.L. and Kounaves, S.P. (2015) The origins of perchlorate in the Martian soil.
844 *Geophys. Res. Lett.* **42**, 3739-3745.
- 845 Cassata, W.S., Cohen, B.E., Mark, D.F., Trappitsch, R., Crow, C.A., Wimpenny, J., Lee,
846 M.R. and Smith, C.L. (2018) Chronology of martian breccia NWA 7034 and the formation
847 of the martian crustal dichotomy. *Sci. Adv.* **4**, eaap8306.
- 848 Catling, D.C. and Kasting, J.F. (2017) Atmospheric Evolution on Inhabited and Lifeless
849 Worlds. Cambridge University Press, Cambridge, United Kingdom. 579 p.
- 850 Catling, D.C. and Zahnle, K.J. (2020) The Archean atmosphere. *Sci. Adv.* **6**, eaax1420.
- 851 Chen, M., Campbell, I.H., Xue, Y., Tian, W., Ireland, T.R., Holden, P., Cas, R.A.F., Hayman,
852 P.C. and Das, R. (2015) Multiple sulfur isotope analyses support a magmatic model for the
853 volcanogenic massive sulfide deposits of the Teutonic Bore Volcanic Complex, Yilgarn
854 Craton, Western Australia. *Econ. Geol.* **110**, 1411-1423.

855 Christensen, P.R. and Ruff, S.W. (2004) Formation of the hematite- bearing unit in
856 Meridiani Planum: Evidence for deposition in standing water. *J. Geophys. Res. – Planet.*
857 **109**, E08003.

858 Cohen, B.E., Mark, D.F., Cassata, W.S., Lee, M.R., Tomkinson, T. and Smith, C.L. (2017)
859 Taking the pulse of Mars via dating of a plume-fed volcano. *Nature Comm.* **8**, 640.

860 DeWitt, H.L., Hasenkopf, C.A., Trainer, M.G., Farmer, D.K., Jimenez, J.L., McKay, C.P.,
861 Toon, O.B. and Tolbert, M.A. (2010) The formation of sulfate and elemental sulfur
862 aerosols under varying laboratory conditions: Implications for early Earth. *Astrobiology*
863 **10**, 773-781.

864 Ding, T., Valkiers, S., Kipphardt, H., De Bièvre, P., Taylor, P.D.P., Gonfiantini, R. and
865 Krouse, R. (2001) Calibrated sulfur isotope abundance ratios of three IAEA sulfur isotope
866 reference materials and V-CDT with a reassessment of the atomic weight of sulfur.
867 *Geochim. Cosmochim. Acta* **65**, 2433-2437.

868 Dottin III, J.W., Labidi, J., Farquhar, J., Piccoli, P., Liu, M.-C. and McKeegan, K.D. (2018)
869 Evidence for oxidation at the base of the nakhlite pile by reduction of sulfate salts at the
870 time of lava emplacement. *Geochim. Cosmochim. Acta* **239**, 186-197.

871 Endo, Y., Danielache, S.O., Ueno, Y., Hattori, S., Johnson, M.S., Yoshida, N., and
872 Kjaergaard, H.G. (2015) Photoabsorption cross-section measurements of ³²S, ³³S, ³⁴S, and
873 ³⁶S sulfur dioxide from 190 to 220nm. *J. Geophys. Res. – Planet.* **120**, 2546–2557.

874 Endo, Y., Danielache, S.O. and Ueno, Y. (2019) Total pressure dependence of sulfur mass-
875 independent fractionation by SO₂ photolysis. *Geophys. Res. Lett.* **46**, 483–491.

876 Endo, Y., Ueno, Y., Aoyama, S., and Danielache, S.O. (2016). Sulfur isotope fractionation by
877 broadband UV radiation to optically thin SO₂ under reducing atmosphere. *Earth Planet.*
878 *Sci. Lett.* **453**, 9–22.

879 Farquhar, J., Bao, H. and Thiemens, M. (2000a) Atmospheric influence of Earth’s earliest
880 sulfur cycle. *Science* **289**, 756-758.

881 Farquhar, J., Johnston, D.T. and Wing, B.A. (2007a) Implications of conservation of mass
882 effects on mass-dependent isotope fractionations: Influence of network structure on sulfur
883 isotope phase space of dissimilatory sulfate reduction. *Geochim. Cosmochim. Acta* **71**,
884 5862–5875.

885 Farquhar, J., Kim, S.-T. and Masterson, A. (2007b) Implications from sulfur isotopes of the
886 Nakhla meteorite for the origin of sulfate on Mars. *Earth Planet. Sci. Lett.* **264**, 1-8.

887 Farquhar, J., Savarino, J., Airieau, S. and Thiemens, M.H. (2001) Observation of
888 wavelength- sensitive mass- independent sulfur isotope effects during SO₂ photolysis:
889 Implications for the early atmosphere. *J. Geophys. Res. – Planet.* **106**, 32829-32839.

890 Farquhar, J., Savarino, J., Jackson, T.L. and Thiemens, M.H. (2000b) Evidence of
891 atmospheric sulphur in the Martian regolith from sulphur isotopes in meteorites. *Nature*
892 **404**, 50-52.

893 Farquhar, J. and Wing, B.A. (2003) Multiple sulfur isotopes and the evolution of the
894 atmosphere. *Earth Planet. Sci. Lett.* **213**, 1-13.

895 Farquhar, J., Zerkle, A.L. and Bekker, A. (2014) Geologic and geochemical constraints on
896 Earth’s early atmosphere. in: Holland, H., Turekian, K.K. (Eds.), *Treatise in*
897 *Geochemistry*, Vol. 6: The Atmosphere, pp. 91-138.

898 Franz, H.B., Kim, S.-T., Farquhar, J., Day, J.M.D., Economos, R.C., McKeegan, K.D.,
899 Schmitt, A.K., Irving, A.J., Hoek, J. and Iii, J.D. (2014) Isotopic links between
900 atmospheric chemistry and the deep sulphur cycle on Mars. *Nature* **508**, 364-368.

901 Franz, H.B., McAdam, A.C., Ming, D.W., Freissinet, C., Mahay, P.R., Eldridge, D.L.,
902 Fischer, W.W., Grotzinger, J.P., House, C.H., Hurowitz, J.A., McLennan, S.M.,
903 Schwenzer, S.P., Vaniman, D.T., Archer Jr., P.D., Atreya, S.K., Conrad, P.G., Dottin III,
904 J.W., Eigenbrode, J.L., Farley, K.A., Glavin, D.P., Johnson, S.S., Knudson, C.A., Morris,

905 R.V., Navarro-González, R., Pavlov, A.A., Plummer, R., Rampe, E.B., Stern, J.C., Steele,
906 A., Summons, R.E. and Sutter, B. (2017) Large sulfur isotope fractionations in Martian
907 sediments at Gale crater. *Nature Geosci.* **10**, 658-662.

908 Franz, H.B., Wu, N., Farquhar, J. and Irving, A.J. (2014) A new type of isotopic anomaly in
909 shergottite sulfides. *Meteorit. Planet. Sci.* **54**, 3036-3051.

910 Gaillard, F., Michalski, J., Berger, G., McLennan, S.M. and Scaillet, B. (2013) Geochemical
911 reservoirs and timing of sulfur cycling on Mars. *Space Sci. Rev.* **174**, 251-300.

912 Gaillard F., Scaillet, B. and Arndt, N.T. (2011) Atmospheric oxygenation caused by a change
913 in volcanic degassing pressure. *Nature* **478**, 229-232.

914 Gaillard, F. and Scaillet, B. (2009) The sulfur content of volcanic gases on Mars. *Earth*
915 *Planet. Sci. Lett.* **279**, 34-43.

916 Gattacceca, J., Rochette, P., Scorzelli, R.B., Munayco, P., Agee, C., Quesnel, Y., Cournède,
917 C. and Geissman, J. (2014) Martian meteorites and Martian magnetic anomalies: A new
918 perspective from NWA 7034. *Geophys. Res. Lett.* **41**, 4859-4864.

919 Glaze, L.S. and Baloga, S.M. (2002) Volcanic plume heights on Mars: Limits of validity for
920 convective models. *J. Geophys. Res.* **107**, E10.

921 Goderis, S., Brandon, A.D., Mayer, B. and Humayun, M. (2016) Ancient impactor
922 components preserved and reworked in martian regolith breccia Northwest Africa 7034.
923 *Geochim. Cosmochim. Acta* **191**, 203-215.

924 Gough, R.V., Chevrier, V.F., Baustian, K.J., Wise, M.E. and Tolbert, M.A. (2011)
925 Laboratory studies of perchlorate phase transitions: Support for metastable aqueous
926 perchlorate solutions on Mars. *Earth Planet. Sci. Lett.* **312**, 371-377.

927 Greenwood, J.P., Mojzsis, S.J. and Coath, C.D. (2000) Sulfur isotopic compositions of
928 individual sulfides in Martian meteorites ALH84001 and Nakhla: Implications for crust-
929 regolith exchange on Mars. *Earth Planet. Sci. Lett.* **184**, 23-35.

930 Groves, D.I., Korzikowski, E.A., McNaughton, N.J., Leshner, C.M. and Cowden, A. (1986)
931 Thermal erosion by komatiites at Kambalda, Western Australia and the genesis of nickel
932 ores. *Nature* **319**, 136-139.

933 Haberle, R.M., Catling, D.C., Forget, F., Smith, M.D. and Zurek, R.W. (2017) The early
934 Mars climate system, in: Haberle, R.M., Clancy, R.T., Forget, F., Smith, M.D., Zurek,
935 R.W. (Eds.), *The Atmosphere and Climate of Mars*. Cambridge University Press,
936 Cambridge, United Kingdom, pp. 526-568.

937 Harman, C.E., Pavlov, A.A., Babikov, D. and Kasting, J.F. (2018) Chain formation as a
938 mechanism for mass-independent fractionation of sulfur isotopes in the Archean
939 atmosphere. *Earth Planet. Sci. Lett.* **496**, 238-247.

940 Herd, C.D.K., Walton, E.L., Agee, C.B., Mutik, N., Ziegler, K., Shearer, C.K., Bell, A.S.,
941 Santos, A.R., Burger, P.V., Simon, J.I., Tappa, M.J., McCubbin, F.W., Gattacceca, J.,
942 Lacroix, F., Sanborn, M.E., Yin, Q.-Z., Cassata, W.S., Borg, L.E., Lindvall, R.E., Kruijjer,
943 T.S., Brennecka, G.A., Kleine, T., Nishiizumi, K. and Caffee, M.W. (2017) The
944 Northwest Africa 8159 martian meteorite: Expanding the martian sample suite to the early
945 Amazonian. *Geochim. Cosmochim. Acta* **218**, 1-26.

946 Hewins, R.H., Zanda, B., Humayun, M., Nemchin, A., Lorand, J.-P., Pont, S., Deldicque, D.,
947 Bellucci, J.J., Beck, P., Leroux, H., Marinova, M., Remusat, L., Göpel, C., Lewin, E.,
948 Grange, M., Kennedy, A. and Whitehouse, M.J. (2017) Regolith breccia Northwest Africa
949 7533: Mineralogy and petrology with implications for early Mars. *Meteorit. Planet. Sci.*
950 **52**, 89-124.

951 Humayun, M., Nemchin, A., Zanda, B., Hewins, R.H., Grange, M., Kennedy, A., Lorand,
952 J.P., Göpel, C., Fieni, C., Pont, S. and Deldicque, D. (2013) Origin and age of the earliest
953 Martian crust from meteorite NWA7533. *Nature* **503**, 513-516.

954 Hynek, B. (2016) The great climate paradox of ancient Mars. *Geology* **44**, 879-880.

- 955 Izon, G., Zerkle, A.L., Williford, K.H., Farquhar, J., Poulton, S.W. and Claire, M.W. (2017)
956 Bi-ological regulation of atmospheric chemistry en route to planetary oxygenation. *Proc.*
957 *Natl. Acad. Sci.* **114**, E2571–E2579.
- 958 Jamieson, J.W., Wing, B.A., Farquhar, J. and Hannington, M.D. (2013) Neoproterozoic seawater
959 6 sulphate concentrations from sulphur isotopes in massive sulphide ore. *Nat. Geosci.* **6**,
960 61-7 64.
- 961 Keller, J.M., Boynton, W.V., Karunatillake, S., Baker, V.R., Dohm, J.M., Evans, L.G., Finch,
962 M.J., Hahn, B.C., Hamara, D.K., Janes, D.M., Kerry, K.E., Newsom, H.E., Reedy, R.C.,
963 Sprague, A.L., Squyres, S.W., Starr, R.D., Taylor, G.J. and Williams, R.M.S. (2006)
964 Equatorial and midlatitude distribution of chlorine measured by Mars Odyssey GRS. *J.*
965 *Geophys. Res. – Planet.* **111**, E03S08.
- 966 Kite, E.S. (2019) Geologic constraints on early Mars climate. *Space Sci Rev* **215**, 10.
- 967 Krysztofiak, G., Té, Y.V., Catoire, V., Berthet, G., Toon, G.C., Jégou, F., Jeseck, P. and
968 Robert, C. (2015) Carbonyl Sulphide (OCS) variability with latitude in the atmosphere,
969 *Atmos.-Ocean* **53**, 89-101.
- 970 Labidi, J. and Cartigny, P. (2016) Negligible sulfur isotope fractionation during partial
971 melting: Evidence from Garrett transform fault basalts, implications for the late-veener
972 and the hadean matte. *Earth Planet. Sci. Lett.* **451**, 196-207.
- 973 Laflamme, C., Martin, L., Jeon, H., Reddy, S.M., Selvaraja, V., Caruso, S., Bui, T.H.,
974 Roberts, M.P., Voute, F., Hagemann, S., Wacey, D., Littman, S., Wing, B., Fiorentini, M.
975 and Kilburn, M.R. (2016) In situ multiple sulfur isotope analysis by SIMS of pyrite,
976 chalcopyrite, pyrrhotite, and pentlandite to refine magmatic ore genetic models. *Chem.*
977 *Geol.* **444**, 1-15.
- 978 Lanza, N.L., Wiens, R.C., Arvidson, R.E., Clark, B.C., Fischer, W.W., Gellert, R.,
979 Grotzinger, J.P., Hurowitz, J.A., McLennan, S.M., Morris, R.V., Rice, M.S., Bell, J.F.,
980 Berger, J.A., Blaney, D.L., Bridges, N.T., Calef, F., Campbell, J.L., Clegg, S.M., Cousin,
981 A., Edgett, K.S., Fabre, C., Fisk, M.R., Forni, O., Frydenvang, J., Hardy, K.R., Hardgrove,
982 C., Johnson, J.R., Lasue, J., Le Mouélic, S., Malin, M.C., Mangold, N., Martín-Torres, J.,
983 Maurice, S., McBride, M.J., Ming, D.W., Newsom, H.E., Ollila, A.M., Sautter, V.,
984 Schröder, S., Thompson, L.M., Treiman, A.H., Vanbommel, S., Vaniman, D.T. and
985 Zorzano, M.-P. (2016) Oxidation of manganese in an ancient aquifer, Kimberley
986 Formation, Gale Crater, Mars. *Geophys. Res. Lett.* **43**, 7398-7407.
- 987 Lapan, T.J., Richter, M., Andreasen, R., Irving, A.J., Satkoski, A.M., Beard, B.L.,
988 Nishiizumi, K., Jull, A.J.T. and Caffee, M.W. (2017) Two billion years of magmatism
989 recorded from a single Mars meteorite ejection site. *Sci. Adv.* **3**, e1600922.
- 990 Lasue, J., Clifford, S.M., Conway, S.J., Mangold, N. and Butcher, F.E.G. (2019) The
991 hydrology of Mars including a potential cryosphere, in: Filiberto, J., Schwenzer, S.P.
992 (Eds.), Volatiles in the Martian crust. Elsevier, pp. 185-246.
- 993 Lin, Y., Sim, M.S. and Ono, S. (2011) Multiple-sulfur isotope effects during photolysis of
994 carbonyl sulfide. *Atmos. Chem. Phys.* **11**, 10283–10292.
- 995 Lorand, J.P., Hewins, R.H., Humayun, M., Remusat, L., Zanda, B., La, C. and Pont, S.
996 (2018) Chalcophile-siderophile element systematics of hydrothermal pyrite from martian
997 regolith breccia NWA 7533. *Geochim. Cosmochim. Acta* **241**, 134-149.
- 998 Lorand, J.P., Hewins, R.H., Remusat, L., Zanda, B., Pont, S., Leroux, H., Marinova, M.,
999 Jacob, D., Humayun, M., Nemchin, A., Grange, M., Kennedy, A. and Gopel, C. (2015)
1000 Nickeliferous pyrite tracks pervasive hydrothermal alteration in Martian regolith breccia:
1001 A study in NWA 7533. *Meteorit. Planet. Sci.* **50**, 2099-2120.
- 1002 Mahaffy, P.R., Webster, C.R., Atreya, S.K., Franz, H., Wong, M., Conrad, P.G., Harpold, D.,
1003 Jones, J.J., Leshin, L.A., Manning, H., Owen, T., Pepin, R.O., Squyres, S. and Trainer, M.

- 1004 (2013) Abundance and isotopic composition of gases in the Martian atmosphere from the
1005 Curiosity Rover. *Science* **341**, 263-266.
- 1006 Mari, N., Riches, A.J.V., Hallis, L.J., Marrocchi, Y., Villeneuve, J., Gleissner, P., Becker, H.
1007 and Lee, M.R. (2019) Syneruptive incorporation of martian surface sulphur in the nakhlite
1008 lava flows revealed by S and Os isotopes and highly siderophile elements: Implication for
1009 mantle sources in Mars. *Geochim. Cosmochim. Acta* **266**, 416-434.
- 1010 McCubbin, F.M., Boyce, J.W., Novak-Szabo, T., Santos, A.R., Tartese, R., Muttik, N.,
1011 Domokos, G., Vazquez, J., Keller, L.P., Moser, D.E., Jerolmack, D.J., Shearer, C.K.,
1012 Steele, A., Elardo, S.M., Rahman, Z., Anand, M., Delhaye, T. and Agee, C. (2016)
1013 Geologic history of Martian regolith breccia Northwest Africa 7034: Evidence for
1014 hydrothermal activity and lithologic diversity in the Martian crust. *J. Geophys. Res. –*
1015 *Planet.* **121**, 2120-2149.
- 1016 McSween Jr., H.Y. and McLennan, S.M. (2014) Mars, in: Davis, A.M. (Ed.), Treatise on
1017 Geochemistry, Volume 2: Planets, Asteroids, Comets and The Solar System. Elsevier
1018 Science, pp. 250-300.
- 1019 Michalski, J.R., Onstott, T.C., Mojzsis, S.J., Mustard, J., Chan, Q.H.S., Niles, P.B. and
1020 Johnson, S.S. (2017) The Martian subsurface as a potential window into the origin of life.
1021 *Nature Geosci.* **11**, 21–26.
- 1022 Mitra, K., & Catalano, J. G. (2019). Chlorate as a potential oxidant on Mars: Rates and
1023 products of dissolved Fe(II) oxidation. *J. Geophys. Res.: Planets* **124**.
1024 <https://doi.org/10.1029/2019JE006133>.
- 1025 Muller, E., Philippota, P., Rollion-Barda, C. and Cartigny, P. (2016) Multiple sulfur-isotope
1026 signatures in Archean sulfates and their implications for the chemistry and dynamics of
1027 the early atmosphere. *Proc. Nat. Acad. Sci.* **113**, no. 27.
- 1028 Muttik, N., McCubbin, F.M., Keller, L.P., Santos, A.R., McCutcheon, W.A., Provencio, P.P.,
1029 Rahman, Z., Shearer, C.K., Boyce, J.W. and Agee, C.B. (2014) Inventory of H₂O in the
1030 ancient Martian regolith from Northwest Africa 7034: The important role of Fe oxides.
1031 *Geophys. Res. Lett.* **41**, 8235–8244.
- 1032 Nuding, D.L., Rivera-Valentin, E.G., Davis, R.D., Gough, R.V., Chevrier, V.F. and Tolbert,
1033 M.A. (2014) Deliquescence and efflorescence of calcium perchlorate: An investigation of
1034 stable aqueous solutions relevant to Mars. *Icarus* **243**, 420-428.
- 1035 O'Neill, H.S.C. & Mavrogenes, J.A. (2002) The sulfide capacity and the sulfur content at
1036 sulfide saturation of silicate melts at 1400°C and 1 bar. *J. Pet.* **43**, 1049-1087.
- 1037 Oppenheimer, C., Scaillet, B., Martin, R.S. (2011) Sulfur degassing from volcanoes: Source
1038 conditions, surveillance, plume chemistry and earth system impacts. *Rev. Mineral.*
1039 *Geochem.* **73**, 363–421.
- 1040 Pavlov, A.A. and Kasting, J.F. (2002) Mass-independent fractionation of sulfur isotopes in
1041 Archean sediments: Strong evidence for an anoxic Archean atmosphere. *Astrobiology* **2**,
1042 27-41.
- 1043 Planavsky, N.J., Asael, D., Hofmann, A., Reinhard, C.T., Lalonde, S.V., Knudsen, A., Wang,
1044 X., Ossa, F.O., Pecoits, E., Smith, A.J.B., Beukes, N.J., Bekker, A., Johnson, T.M.,
1045 Konhauser, K.O., Lyons, T.W. and Rouxel, O.J. (2014) Evidence for oxygenic
1046 photosynthesis half a billion years before the Great Oxidation Event. *Nature Geosci.* **7**,
1047 283-286.
- 1048 Robertson, K. and Bish, D. (2011) Stability of phases in the Mg(ClO₄)₂·nH₂O system and
1049 implications for perchlorate occurrences on Mars. *J. Geophys. Res. – Planet.* **116**, E07006.
- 1050 Santos, A.R., Agee, C.B., McCubbin, F.M., Shearer, C.K., Burger, P.V., Tartese, R. and
1051 Anand, M. (2015) Petrology of igneous clasts in Northwest Africa 7034: Implications for
1052 the petrologic diversity of the martian crust. *Geochim. Cosmochim. Acta* **157**, 56-85.

- 1053 Schwenzer, S.P., Bridges, J.C., Wiens, R.C., Conrad, P.G., Kelley, S.P., Leveille, R.,
1054 Mangold, N., Martín-Torres, J., McAdam, A., Newsom, H., Zorzano, M.P., Rapin, W.,
1055 Spray, J., Treiman, A.H., Westall, F., Fairén, A.G. and Meslin, P.-Y. (2016) Fluids during
1056 diagenesis and sulfate vein formation in sediments at Gale crater, Mars. *Meteorit. Planet.*
1057 *Sci.* **51**, 2175–2202.
- 1058 Shearer, C.K., Bell, A.S., Herd, C.D.K., Burger, P.V., Provencio, P., Sharp, Z.D. and Papike,
1059 J.J. (2019) The Northwest Africa 8159 (NWA 8159) Martian Meteorite Part 2. Spinel-
1060 orthopyroxene intergrowths. A record of fO₂ and crust-basalt interactions. *Geochim.*
1061 *Cosmochim. Acta* **258**, 242–257.
- 1062 Sholes, S.F., Smith, M.L., Claire, M.W., Zahnle, K.J. and Catling, D.C. (2017) Anoxic
1063 atmospheres on Mars driven by volcanism: Implications for past environments and life.
1064 *Icarus* **290**, 46–62.
- 1065 Sossi, P.A. and O'Neill, H.S.C. (2016) Liquidus temperatures of komatiites and the effect of
1066 cooling rate on element partitioning between olivine and komatiitic melt. *Contrib. Min.*
1067 *Pet.* **171**, 49.
- 1068 Squires, S.W., Grotzinger, J.P., Arvidson, R., Bell III, J.F., Calvin, W., Christensen, P.R.,
1069 Clark, B.C., Crisp, J.A., Farrand, W.H., Herkenhoff, K.E., Johnson, J.R., Klingelhofer, G.,
1070 Knoll, A.H., McLennan, S.M., McSween Jr., H.Y., Morris, R.V., Rice, J.W., Rieder, R. and
1071 Soderblom, L.A. (2004) In Situ Evidence for an Ancient Aqueous Environment at
1072 Meridiani Planum, Mars. *Science* **306**, 1709–1714.
- 1073 Stern, J.C., Sutter, B., Jackson, W.A., Navarro-González, R., McKay, C.P., Ming, D.W.,
1074 Archer, P.D. and Mahaffy, P.R. (2017) The nitrate/(per)chlorate relationship on Mars.
1075 *Geophys. Res. Lett.* **44**, 2643–2651.
- 1076 Stoffler, D., Keil, K. and Scott, E.R.D. (1991) Shock metamorphism of ordinary chondrites.
1077 *Geochim. Cosmochim. Acta* **55**, 3845–3867.
- 1078 Tomkins, A.G., Genge, M.J., Tait, A.W., Alkemade, S.L., Langendam, A.D., Perry, P.V. and
1079 Wilson, S.A. (2019) High survivability of micrometeorites on Mars: Sites with enhanced
1080 availability of limiting nutrients. *J. Geophys. Res. – Planet.* **124**
1081 <https://doi.org/10.1029/2019JE006005>
- 1082 Toner, J.D. and Catling, D.C. (2018) Chlorate brines on Mars: Implications for the
1083 occurrence of liquid water and deliquescence. *Earth Planet. Sci. Lett.* **497**, 161–168.
- 1084 Udry, A. and Day, J.M.D. (2018) 1.34 billion-year-old magmatism on Mars evaluated from
1085 the co-genetic nakhlite and chassignite meteorites. *Geochim. Cosmochim. Acta* **238**, 292-
1086 315.
- 1087 Ueno, Y., Johnson, M.S., Danielache, S.O., Eskebjerg, C., Pandey, A., and Yoshida, N.
1088 (2009) Geological sulfur isotopes indicate elevated OCS in the Archean atmosphere,
1089 solving faint young sun paradox. *Proc. Nat. Acad. Sci.* **106**, 14784–14789.
- 1090 Whitehill, A.R., Jiang, B., Guo, H. and Ono, S. (2015) SO₂ photolysis as a source for sulfur
1091 mass-independent isotope signatures in stratospheric aerosols. *Atmos. Chem. Phys.* **15**,
1092 1843–1864.
- 1093 Williams, D.A., Greeley, R., Hauber, E., Gwinner, K. and Neukum, G. (2005) Erosion by
1094 flowing Martian lava: New insights for Hecates Tholus from Mars Express and MER data.
1095 *J. Geophys. Res. – Planet.* **110**, E05006.
- 1096 Williams, J.T., Shearer, C.K., Sharp, Z.D., Burger, P.V., McCubbin, F.M., Santos, A.R.,
1097 Agee, C.B. and McKeegan, K.D. (2016) The chlorine isotopic composition of Martian
1098 meteorites 1: Chlorine isotope composition of Martian mantle and crustal reservoirs and
1099 their interactions. *Meteorit. Planet. Sci.* **51**, 2092–2110.
- 1100 Wilson, L. and Head, J.W. (2007) Explosive volcanic eruptions on Mars: Tephra and
1101 accretionary lapilli formation, dispersal and recognition in the geologic record. *J. Volc.*
1102 *Geotherm. Res.* **163**, 83–97.

1103 Wittman, A., Korotev, R.L., Jolliff, B.L., Irving, A.J., Moser, D.E., Barker, I. and Rumble III,
1104 D. (2015) Petrography and composition of Martian regolith breccia meteorite Northwest
1105 Africa 7475. *Meteorit. Planet. Sci.* **50**, 326-352.
1106 Wordsworth, R.D. (2016) The Climate of Early Mars. *Ann. Rev. Earth Planet. Sci.* **44**, 1-31.
1107 Yang, S., Humayun, M., Righter, K., Jefferson, G., Fields, D. and Irving, A.J. (2015)
1108 Siderophile and chalcophile element abundances in shergottites: Implications for Martian
1109 core formation. *Meteorit. Planet. Sci.* **50**, 691-714.
1110 Zahnle, K., Claire, M. and Catling, D. (2006) The loss of mass-independent fractionation in
1111 sulfur due to a Palaeoproterozoic collapse of atmospheric methane. *Geobiology* **4**, 271-
1112 283.

1113
1114
1115

1116 Figure Captions

1117

1118 **Figure 1** A comparison between $\Delta^{33}\text{S}$ data for Earth and Mars as a function of time.

1119

1120 **Figure 2** Examples of the distribution and petrography of pyrite in Martian polymict
1121 breccias NWA 8171 (A-C) and NWA 11220 (D). A) A broad region of the meteorite
1122 showing the brecciated texture. The distribution of augite is highlighted in light blue
1123 (microprobe mineral map stacked onto a BSE image). B) An example of a larger pyrite grain,
1124 partially replaced by iron oxides (through weathering on Earth), and showing a small analysis
1125 pit remaining after SIMS work. In bright grey can be seen the abundant fine- to medium-
1126 grained magnetite that occurs throughout the sample (the gold remains after polishing off the
1127 coating used in the SIMS analysis). C) The distribution of fine-grained pyrite is highlighted
1128 in bright yellow in this mineral map – BSE image stack. D) Element map of an impact
1129 spherule showing the distribution of sulfur (red), Ca (green) and Mg (blue). An association
1130 between the distribution of some pyrite and calcite filled fractures is clear. In this case, the
1131 larger fractures in the spherule are likely to be contraction cracks formed during cooling.

1132

1133 **Figure 3** Examples of the relationships between pyrrhotite and other minerals in
1134 shergottites examined in this study. A) In this reflected light image of NWA 10170 (paired
1135 with NWA 2990), most pyrrhotite grains are attached to iron-titanium oxides, suggesting that
1136 sulfide saturation was driven by extraction of FeO from the silicate liquid. B) Element map
1137 for NWA 10170, showing the commonly coincident relationships between pyrrhotite
1138 (yellow), apatite (light blue) and ilmenite (small red grains). C) An example of the close
1139 association seen between iron titanium oxides and pyrrhotite typically seen in shergottites
1140 (NWA 7297 in this case; reflected light). Very fine exsolutions of pentlandite can be seen in
1141 the pyrrhotite. D) Stacked element map for Los Angeles. Pyrrhotite is in brightest green,
1142 apatite is in dark green, iron titanium oxides are in red, silicates are in blue. Sulfides are
1143 generally associated with FeTi-oxides or late-crystallising apatite.

1144

1145 **Figure 4** Sulfur isotope data for pyrite in Martian polymict breccia NWA 8171. A) $\Delta^{33}\text{S}$
1146 versus $\delta^{34}\text{S}$; white circles indicate data for 10 μm spots, red spots indicate 7 μm spots, the
1147 yellow diamond indicates the weighted mean of the 10 μm spots, the green diamond is the
1148 shergottite weighted mean from Franz et al. (2019). B) $\Delta^{36}\text{S}$ versus $\delta^{34}\text{S}$; symbols are the
1149 same as in A. C) $\Delta^{36}\text{S}$ versus $\Delta^{33}\text{S}$, the pink shaded area is the previous Mars meteorite data
1150 including 2 σ error bars (from Franz et al., 2014; 2019), and the red-outlined blue square is
1151 the weighted mean error window for our 10 μm spot data, which are overlain. D) Comparison
1152 between the NWA 8171 data (dark blue circles) and those for Archean sulfate (white circles)

1153 on Earth, and sulfides found in sulfate-rich layers (black squares) from [Muller et al. \(2016\)](#).
1154 The green field indicates the experimental results of OCS photolysis under a Xe lamp at $\lambda <$
1155 200 nm (from [Lin et al., 2011](#)); there is close agreement between this and the weighted mean
1156 error window for the NWA 8171 data (red outline).
1157

1158 **Figure 5** $\Delta^{33}\text{S}$ data for Martian meteorites other than NWA 7034 (and pairs). A) Data
1159 for shergottites from this study (blue) and from [Franz et al. \(2014; 2019\)](#) (other shades); the
1160 anomalous shergottites NWA 2290 (and pair NWA5960), Los Angeles, NWA 11300 and
1161 NWA 7635 are indicated. B) Data for the nakhlites from [Franz et al. \(2014; coloured shapes\)](#)
1162 and [Dottin et al. \(2018; grey shapes\)](#), highlighting the three anomalous samples, as well as
1163 the ancient orthopyroxenite ALH84001; the field of all shergottite data is indicated in the
1164 small grey field to highlight the differences in the x and y axes of A and B.
1165

1166 **Figure 6** Schematic illustration of processes affecting the $\Delta^{33}\text{S}$ system on Mars (see
1167 text) (modified from an equivalent diagram for the $\delta^{34}\text{S}$ system in [Franz et al., 2017](#)).
1168

Table 1. Representative electron microprobe analyses of NWA 8171 pyrites.

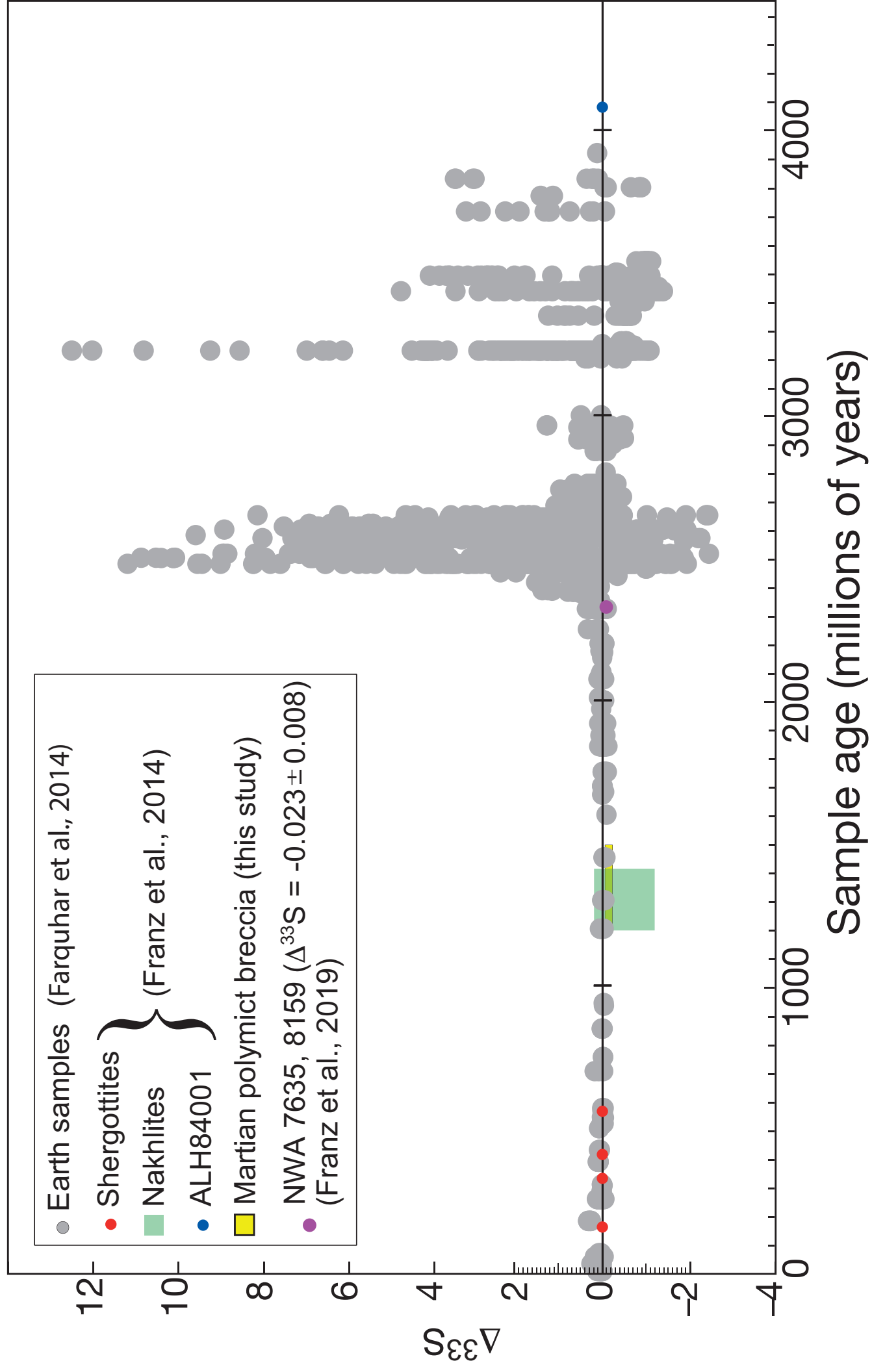
ID - spot	Fe	Ni	S	As	Co	Total
A - 1	45.86	0.10	53.65	b.d.l.	0.02	99.64
B - 1	46.57	0.02	53.41	0.00	0.01	100.03
B - 2	44.11	1.75	53.04	b.d.l.	0.04	98.97
B - 3	43.48	2.23	53.19	b.d.l.	0.05	98.97
C - 1	45.67	0.10	52.36	0.01	0.02	98.17
C - 2	44.13	1.33	52.04	0.01	0.01	97.53
C - 3	44.76	1.04	52.15	b.d.l.	0.03	97.99
E - 1	45.65	0.07	53.37	0.00	0.00	99.12
H - 1	45.92	0.04	53.49	0.01	0.01	99.50
I - 1	43.75	1.39	54.02	b.d.l.	0.22	99.39
K - 1	45.78	b.d.l.	53.47	b.d.l.	b.d.l.	99.24
K - 2	44.69	0.82	53.36	0.01	0.02	98.92
L - 1	44.93	0.52	53.55	b.d.l.	b.d.l.	99.02
L - 2	45.52	0.00	53.58	b.d.l.	b.d.l.	99.12
N - 1	42.23	3.23	52.86	b.d.l.	0.02	98.35
O - 2	45.40	0.09	53.17	0.01	0.00	98.70
P - 1	45.72	0.17	53.63	0.00	b.d.l.	99.54
Q - 2	44.77	0.46	53.53	0.01	0.06	98.85

All data in wt. %.

Table 2. Sulfur isotope data for samples analysed in this study.

Sample	Spot μm	$\delta^{33}\text{S}$	2s	$\delta^{34}\text{S}$	2s	$\delta^{36}\text{S}$	2s	D^{33}S	2s	D^{36}S	2s
NWA 7320	20	-0.22	0.13	-0.43	0.23	-1.35	0.72	-0.01	0.12	-0.53	0.66
NWA 7320	20	-0.20	0.13	-0.38	0.24	-1.39	0.73	0.00	0.12	-0.66	0.68
NWA 7397	20	-0.03	0.13	0.054	0.22	0.40	0.72	-0.06	0.11	0.30	0.65
NWA 7397	20	-0.12	0.14	-0.11	0.23	-0.48	0.76	-0.07	0.13	-0.28	0.72
NWA 7397	20	-0.40	0.16	-0.77	0.28	-2.51	0.84	0.00	0.17	-1.04	0.84
NWA 7397	20	0.02	0.13	0.15	0.23	0.13	0.71	-0.05	0.11	-0.17	0.65
NWA 7397	20	0.09	0.14	0.07	0.24	-0.21	0.76	0.05	0.13	-0.35	0.71
NWA 7397	20	0.09	0.14	0.24	0.23	-0.02	0.72	-0.04	0.12	-0.48	0.67
NWA 7397	20	0.24	0.14	0.59	0.24	0.63	0.73	-0.06	0.13	-0.50	0.68
NWA 7397	20	0.16	0.14	0.11	0.24	-0.17	0.79	0.11	0.14	-0.37	0.75
NWA 7397	20	-0.40	0.16	-0.77	0.28	-2.51	0.84	0.00	0.17	-1.04	0.84
NWA 7397	20	0.02	0.13	0.15	0.23	0.13	0.71	-0.05	0.11	-0.17	0.65
NWA 8656	20	-0.46	0.21	-0.88	0.33	-1.29	0.97	0.00	0.15	0.39	0.90
NWA 8656	20	-0.37	0.21	-0.84	0.34	-2.34	0.97	0.06	0.15	-0.74	0.91
NWA 8656	20	-0.39	0.20	-0.68	0.33	-0.85	0.98	-0.04	0.14	0.46	0.90
NWA 8656	20	-0.59	0.21	-1.20	0.35	-2.32	1.05	0.03	0.16	-0.03	1.01
NWA 8656	20	-0.47	0.20	-0.91	0.31	-1.54	0.97	0.00	0.12	0.19	0.88
NWA 8656	20	-0.20	0.20	-0.42	0.32	0.23	0.94	0.02	0.13	1.03	0.84
NWA 8656	20	-0.36	0.20	-0.85	0.32	-0.82	0.90	0.08	0.13	0.81	0.81
NWA 8656	20	-0.29	0.20	-0.40	0.31	-0.81	0.92	-0.09	0.13	-0.04	0.82
NWA 8656	20	-0.42	0.21	-0.80	0.32	-1.25	0.96	0.00	0.14	0.28	0.87
NWA 8656	20	-0.85	0.22	-1.68	0.35	-2.51	0.97	0.02	0.17	0.70	0.93
NWA 8656	20	-0.70	0.21	-1.29	0.34	-2.84	0.96	-0.04	0.15	-0.37	0.90
NWA 8656	20	-0.55	0.22	-0.96	0.35	-0.82	0.98	-0.06	0.17	1.00	0.94
NWA 8716	20	-0.04	0.21	0.02	0.34	0.71	0.98	-0.05	0.16	0.67	0.91
NWA 8171	10	-1.06	0.22	-1.62	0.37	-4.18	0.94	-0.22	0.28	-1.09	1.21
NWA 8171	10	-0.75	0.20	-1.09	0.37	-2.60	0.98	-0.19	0.26	-0.52	1.23
NWA 8171	10	-1.45	0.24	-2.34	0.36	-4.59	1.09	-0.24	0.29	-0.13	1.32
NWA 8171	10	-0.94	0.20	-1.80	0.36	-4.17	0.88	-0.02	0.26	-0.75	1.15
NWA 8171	10	-1.55	0.20	-2.99	0.38	-6.07	0.94	-0.01	0.27	-0.36	1.22
NWA 8171	10	-0.59	0.21	-0.98	0.38	-2.50	0.95	-0.09	0.27	-0.63	1.23
NWA 8171	10	-0.81	0.19	-1.14	0.33	-2.92	0.90	-0.22	0.24	-0.75	1.13
NWA 8171	10	-2.84	0.16	-5.21	0.31	-11.21	1.07	-0.15	0.21	-1.27	1.26
NWA 8171	10	-0.51	0.19	-0.70	0.37	-2.03	0.94	-0.15	0.25	-0.69	1.21
NWA 8171	7	0.51	0.21	1.02	0.30	2.34	0.85	-0.01	0.19	0.40	0.92
NWA 8171	7	-0.16	0.32	-0.05	0.54	-0.48	1.18	-0.13	0.38	-0.38	1.50
NWA 8171	7	-0.45	0.26	-0.32	0.39	-0.24	0.97	-0.29	0.27	0.36	1.14
NWA 8171	7	-3.07	0.22	-6.09	0.30	-12.37	0.94	0.07	0.20	-0.77	1.01
NWA 8171	7	-0.14	0.25	0.00	0.38	-1.45	0.95	-0.14	0.26	-1.46	1.11

Figure



Figure

[Click here to download high resolution image](#)

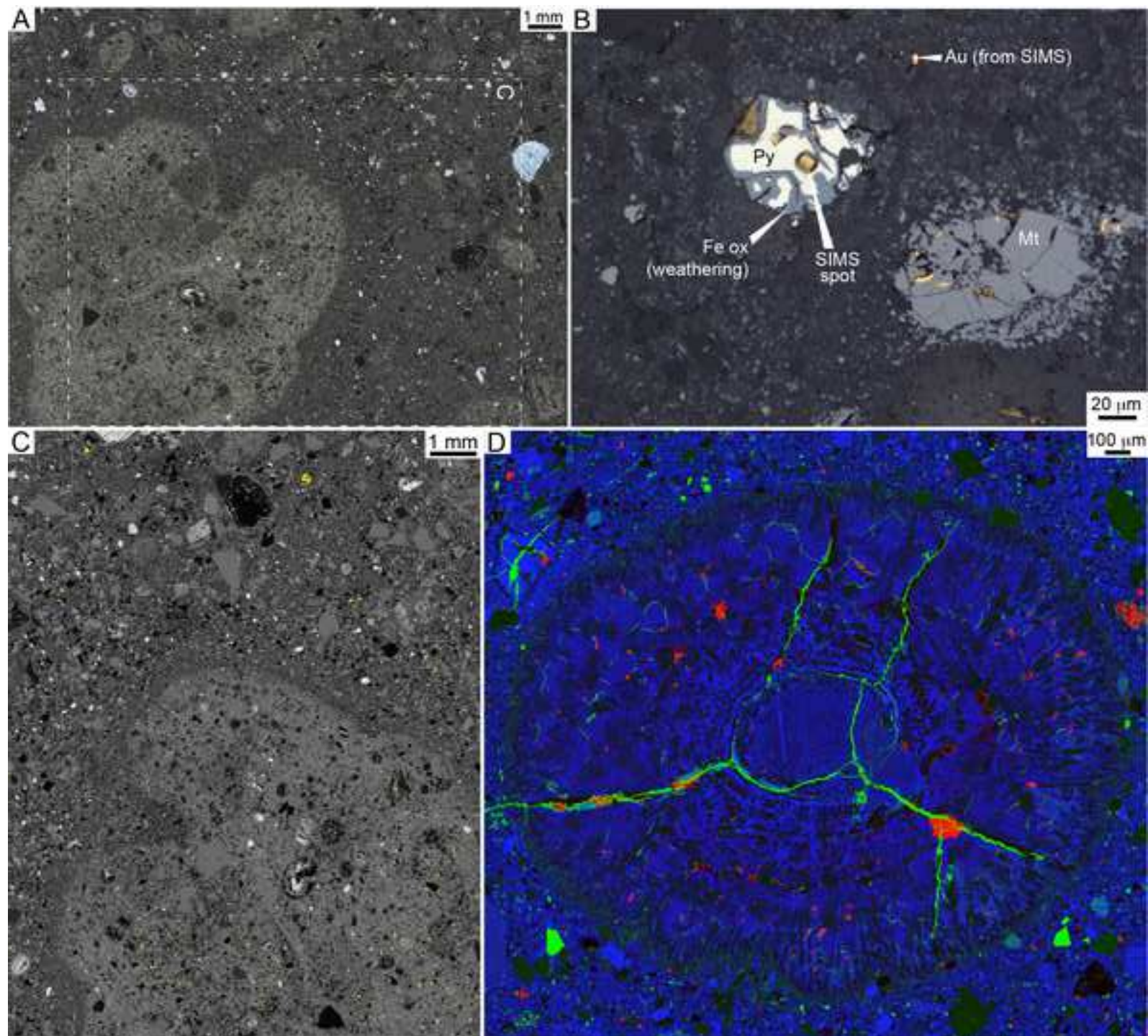
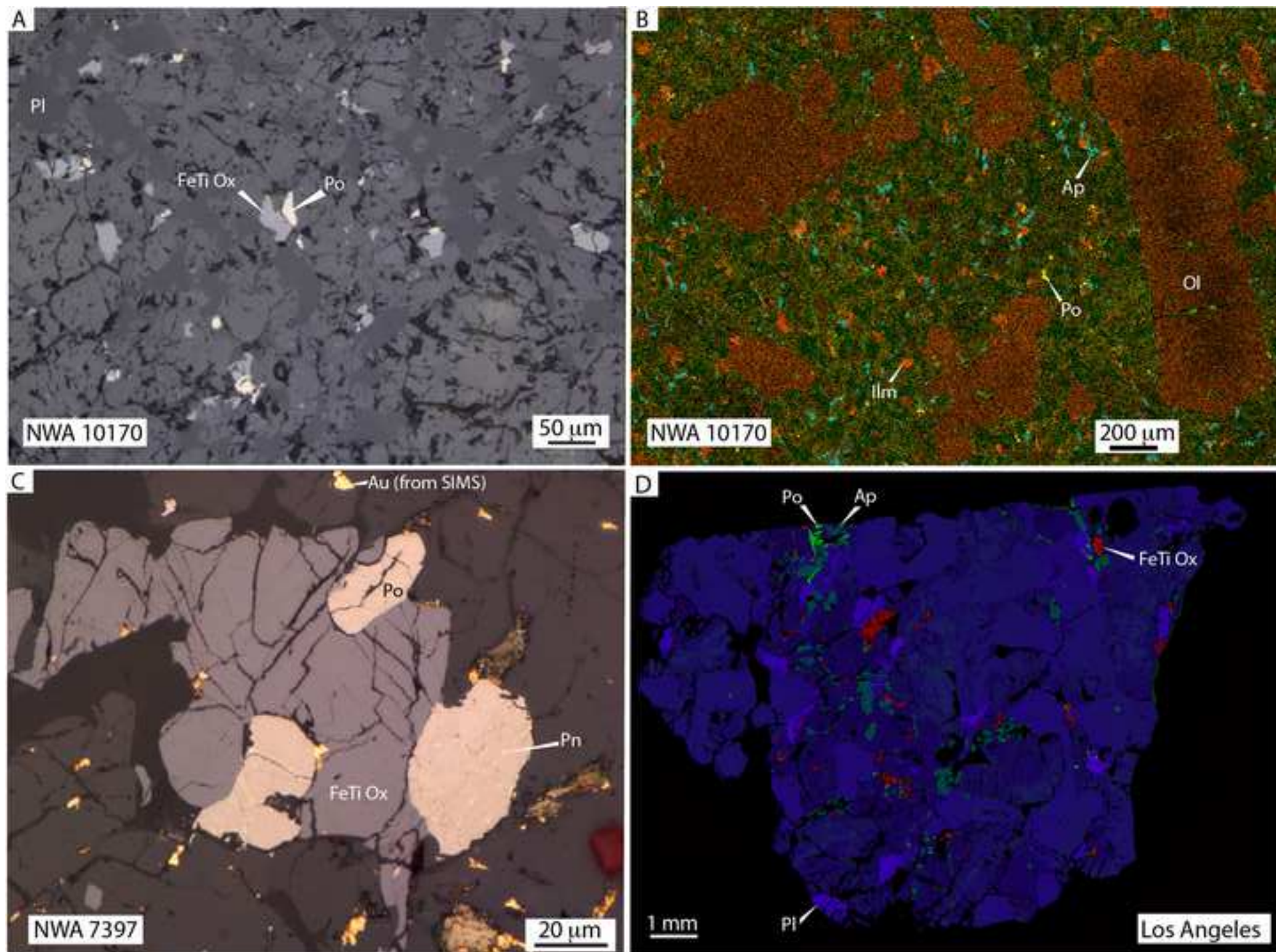
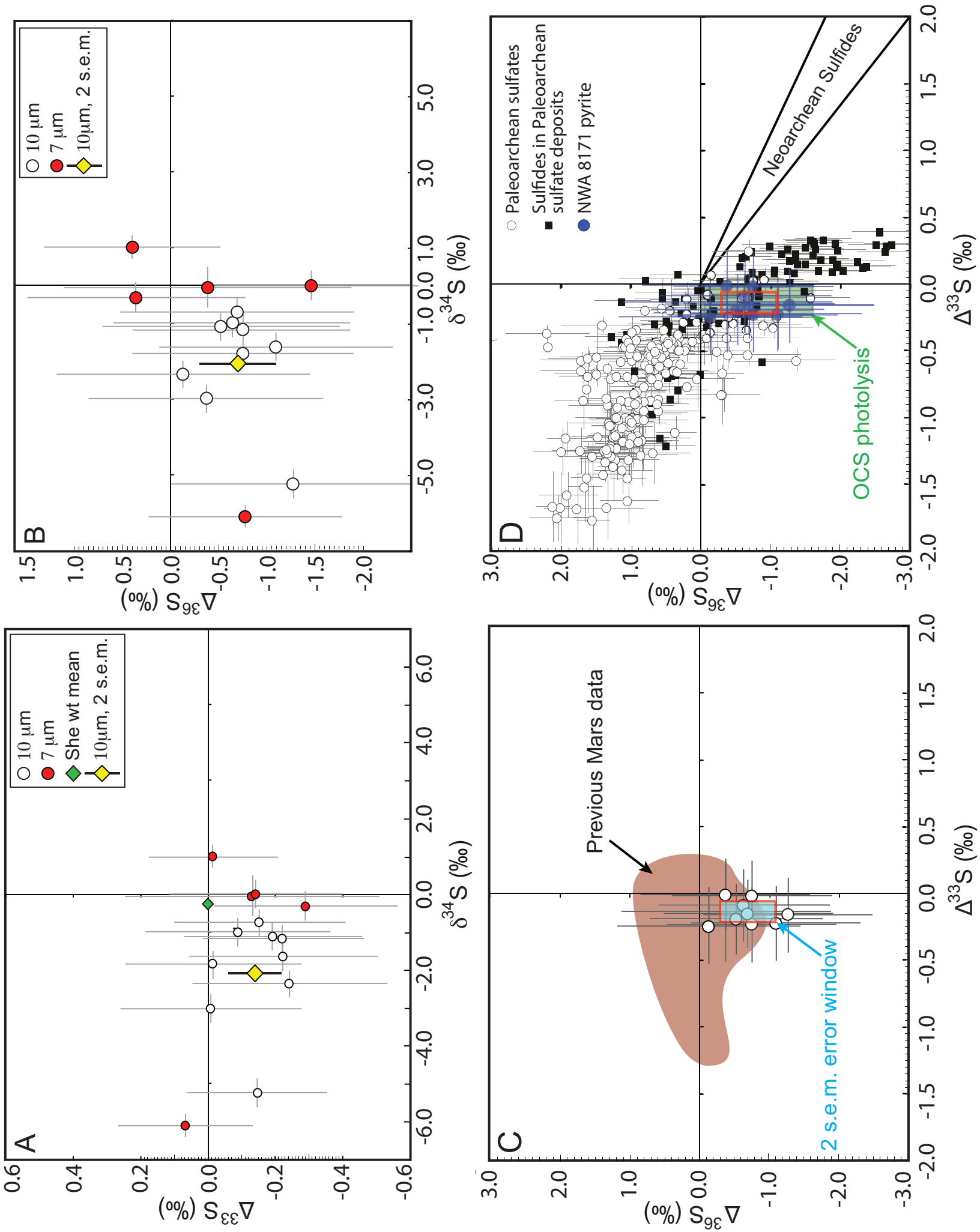


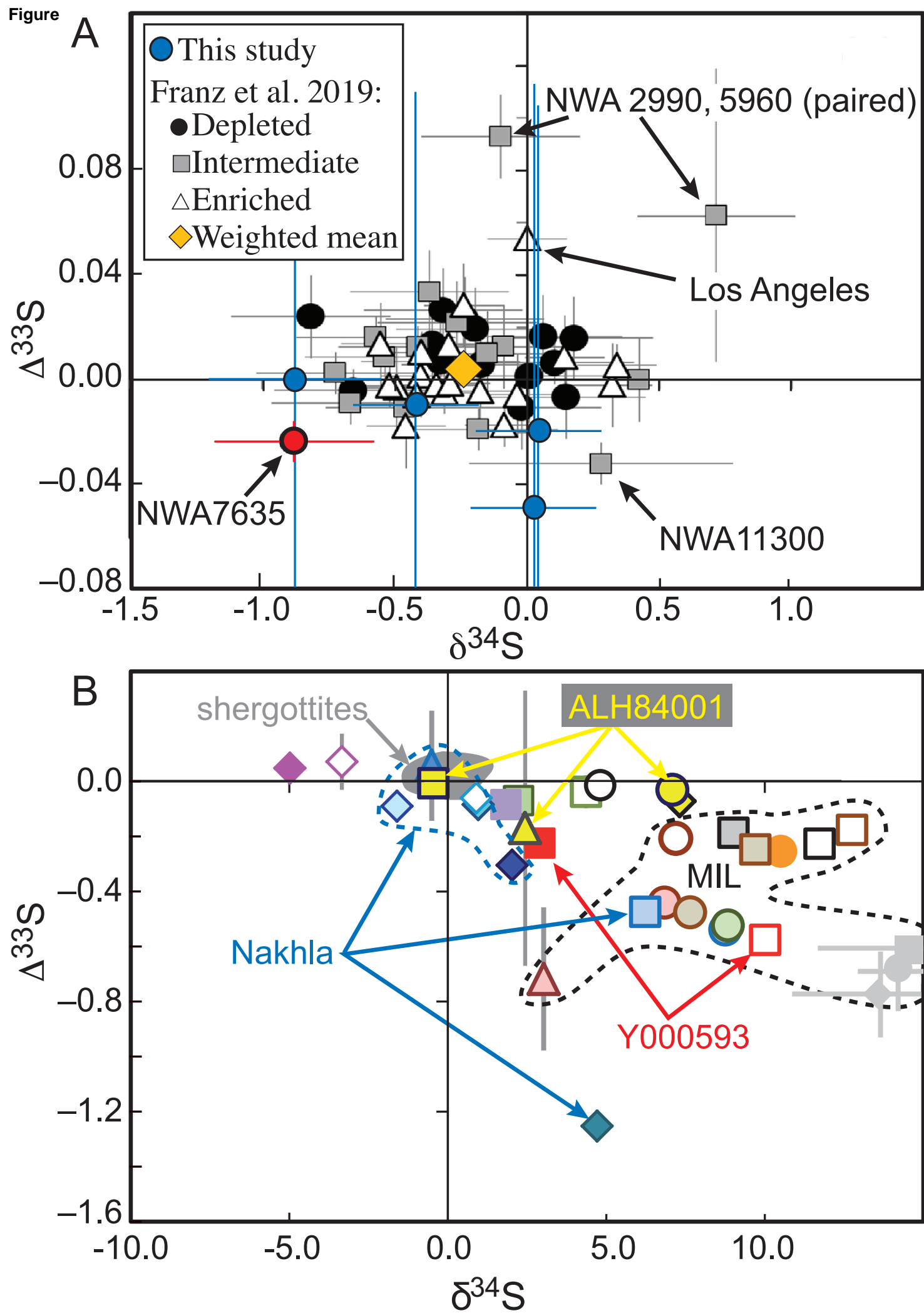
Figure
[Click here to download high resolution image](#)



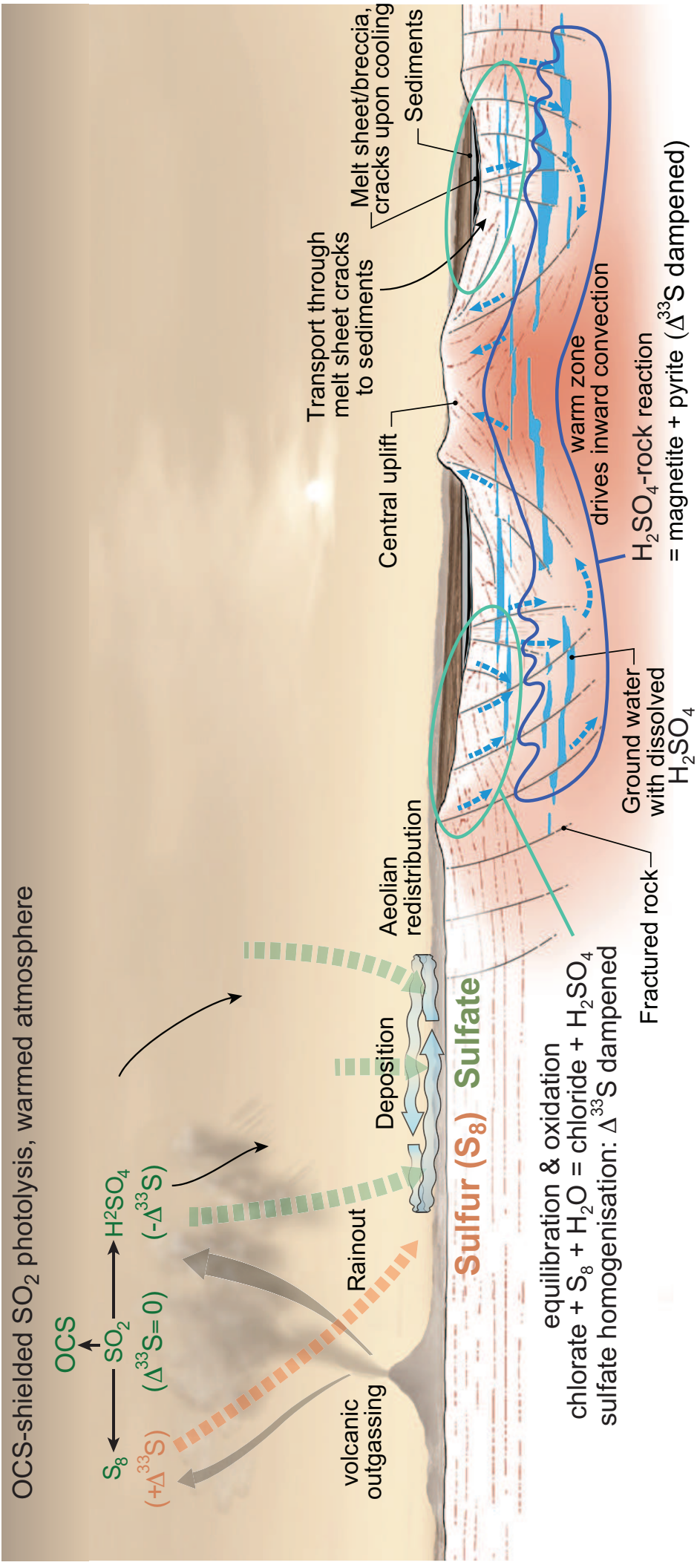
Figure



Figure



Figure



Electronic Annex

[Click here to download Electronic Annex: research data.xlsx](#)

*Declaration of Interest Statement

The authors declare no competing interest.